



Publication Year	2023
Acceptance in OA	2023-05-30T08:43:54Z
Title	Investigating the Effect of Solar Ambient and Data Characteristics on Ca ii K Observations and Line Profile Measurements
Authors	MURABITO, Mariarita, ERMOLLI, Ilaria, CHATZISTERGOS, THEODOSIOS, Jafarzadeh, Shahin, GIORGI, Fabrizio, Rouppe van der Voort, Luc
Publisher's version (DOI)	10.3847/1538-4357/acc529
Handle	http://hdl.handle.net/20.500.12386/34216
Journal	THE ASTROPHYSICAL JOURNAL
Volume	947

Investigating the effect of solar ambient and data characteristics on Ca II K observations and line profile measurements

M. MURABITO,¹ I. ERMOLLI,² T. CHATZISTERGOS,³ S. JAFARZADEH,^{3,4} F. GIORGI,² AND L. ROUPPE VAN DER VOORT^{5,4}

¹*INAF Osservatorio Astronomico di Capodimonte, Salita Moiarriello 16, 80131 Naples, Italy*

²*INAF Osservatorio Astronomico di Roma, Via Frascati 33, 00078 Monte Porzio Catone, Italy*

³*Max Planck Institute for Solar System Research, Justus-von-Liebig-Weg 3, 37077 Göttingen, Germany*

⁴*Roseland Centre for Solar Physics, University of Oslo, P.O. Box 1029 Blindern, 0315 Oslo, Norway*

⁵*Institute of Theoretical Astrophysics, University of Oslo, PO Box 1029, Blindern 0315, Oslo, Norway*

(Received March 31, 2023)

Submitted to ApJ

ABSTRACT

We analysed state-of-the-art observations of the solar atmosphere to investigate the dependence of the Ca II K brightness of several solar features on spectral bandwidth and spatial resolution of the data. Specifically, we study data obtained at the Swedish Solar Telescope with the CRISP and CHROMIS instruments. The analyzed data, which are characterized by spectral bandwidth of 0.12 Å and spatial resolution of 0.078'', were acquired close to disc center by targeting a quiet Sun area and an active region. We convolved the original observations with Gaussian kernels to degrade their spectral bandwidth and spatial resolution to the instrumental characteristics of the most prominent series of Ca II K observations available to date. We then studied the effect of data degradation on the observed regions and on parameters derived from Ca II K line measurements that are largely employed as diagnostics of the solar and stellar chromospheres. We find that the effect of degrading the spectral resolution of Ca II K observations and line profiles depends on both the employed bandwidth and observed solar region. Besides, we found that the spatial degradation impacts the data characterized by a broad bandwidth to a larger extent compared to those acquired with a narrow band. However, the appearance of the observed solar regions is only slightly affected by the spatial resolution of data with bandwidths up to 1 Å and in the range [3,10] Å. Finally, we derived relationships that can be used to intercalibrate results from observations taken with different instruments in diverse regions of the solar atmosphere.

Keywords: Sun: activity – Sun: photosphere – Sun: chromosphere – Sun: faculae, plages – sunspots

1. INTRODUCTION

Solar observations have often served as benchmarks of stellar conditions (Schmelz 2003; Engvold et al. 2019). A particularly illustrative example of the above link is given by the observations in the Ca II H & K lines at 3968.47 Å and 3933.67 Å, respectively, which are the two deepest and broadest absorption lines in the visible spectrum of the Sun.

In fact, early observations of the solar disc at the cores of the Ca II H & K lines revealed brightenings in large regions surrounding sunspots and in a network pattern across the whole solar disc (Hale & Ellerman 1903). Concurrently to these observations, late-type stars were also found to commonly show emissions at the Ca II H & K lines and thus considered to have atmospheric layers similar to those of the Sun (Eberhard & Schwarzschild 1913). Later on, solar observations revealed a clear association between brightening at the Ca II H & K lines and magnetic field strength (Babcock & Babcock 1955; Howard 1959; Chatzistergos et al. 2019) and area (Leighton 1959; Sheeley 1967). Along with previous observations, this association allowed the

Ca II H & K emissions to be used as an indicator of the magnetic fields in the Sun and other stars (Wilson 1978). Since then, measurements at the Ca II H & K lines have widely been used to trace changes in the surface of the Sun and other stars due to magnetic activity and other processes such as rotation and convection (e.g., White & Livingston 1978; Keil & Worden 1984; Noyes et al. 1984; Baliunas 1984; Baliunas et al. 1995; Hall et al. 1995; Radick et al. 1998; Hall et al. 2007; Radick et al. 2018, and references therein).

Furthermore, for many years, the Ca II H & K lines have been used as one of the most reliable diagnostics of the physical properties of the solar (Linsky 1970; Linsky & Avrett 1970) and stellar (?) chromospheres. This is due to the characteristic profile of the Ca II H & K lines, which show two peaks and two secondary minima towards the violet or red part of the spectrum relative to the line centre, and a reversal at the line centre. These line features result from emissions originating from the photosphere, where the temperature decreases with height until a temperature minimum is reached, to the overlying lower chromosphere, where the temperature increases with height (Linsky 1968). Following the notation given by Hale & Ellerman (1903), in the Ca II K line the abovementioned line features are labeled as K_{1V} , K_{1R} , K_{2V} , K_{2R} , and K_3 , respectively. Noteworthy, they all occur within a 1 Å interval and are qualitatively the same for both the quiet Sun and plages regions. However, for the latter the K_{2V} and K_{2R} peaks and the K_3 minimum display a significant intensity increase relative to the quiet Sun (Linsky 1970).

It is worth noting that, although both spectral regions are observable from the ground, the Ca II H & K lines have not been equally explored, with existing observations in favour of the Ca II K line. Contributing to this is that the Ca II H line is blended with the Balmer H ϵ line at 3970.07 Å. Another reason is that Ca II H line is slightly less sensitive than Ca II K as an atmospheric diagnostic. That is because the Ca II H emission peaks are often less pronounced than in the Ca II K ones, thus probing lower heights in the chromosphere. Further information on the formation and diagnostic potential for the solar atmosphere of the Ca II H & K lines can be found in, e.g., Linsky (1970) and Bjørgen et al. (2018).

The literature concerning solar and stellar observations at the Ca II K line is extensive and suggestive of plenty of data available at that radiation. In fact, full-disc spatially-resolved solar observations at the Ca II K line have continuously been performed since 1892 with various telescopes operating at the Ca II K line with bandwidths in the range [0.09,10] Å centered at the line core, and spatial resolution larger

than 1'' (e.g., Chatzistergos et al. 2020, 2022). Most prominent archives of historical Ca II K data are e.g. those of the Meudon (Malherbe et al. 2023), Kodaikanal (Chatzistergos et al. 2019), Mt Wilson (Lefebvre et al. 2005), and Coimbra (Lourenço et al. 2019) Observatories, while the ones for modern data are e.g. those of the Rome (Ermolli et al. 2022) and Kanzelhöhe (Pötzi et al. 2021) Observatories. Besides, since late 1960s the Ca II K line emission integrated over the solar disc has been measured almost daily at e.g. the Kitt Peak and Sacramento Peak sites of the US National Solar Observatory (e.g., White et al. 1998; Scargle et al. 2013), and at the Kodaikanal Observatory in India (e.g., Sivaraman et al. 1987). Furthermore, there are also Ca II K observations at high spectral resolution, on the order of 0.2 Å or better, acquired on spatially resolved regions of the solar disc with a spatial resolution even better than 0.2'', but over limited time-intervals and disc positions. Such data are e.g. those obtained over the last few years at the Swedish Solar Telescope, which are further described in the following.

In addition to the observations described above, since 1960s the disc-integrated Ca II K emission of the Sun and late-type stars has been monitored at the Mt Wilson Observatory (1966–2003, Wilson 1978; Duncan et al. 1991; Baliunas et al. 1995), then at the Lowell Observatory (1994–present, Hall et al. 2007), and more recently with the Potsdam Echelle Polarimetric and Spectroscopic Instrument (PEPSI) of the Large Binocular Telescope (LBT, see e.g. Dineva et al. 2022), with the HARPS-N spectrograph at the Telescopio Nazionale Galileo (TNG, see e.g. Maldonado et al. 2019), and with the photometers on-board e.g. the CoRoT (Michel et al. 2008; Auvergne et al. 2009; Gondoin et al. 2012) and KEPLER (Borucki et al. 2010; Koch et al. 2010) missions.

It is worth noting that, in spite of being widely observed over many years, several aspects of the Ca II H & K emissions in atmosphere of the Sun and other stars are still not fully understood. Examples are the link between the coverage of a stellar disc by magnetic features and the Ca II H & K emissions (see, e.g., Sowmya et al. 2021), and the relationship between Ca II H & K brightening and magnetic field strength (see, e.g., Chatzistergos et al. 2019). These gaps in the knowledge of the Ca II H & K emissions depend on several factors. Firstly, all the available observations report relative photometric data with respect to some standard that is subjective of a biased definition. For example, the disc-resolved solar observations carry information of the brightening at the Ca II K line with respect to an average quiet-Sun emission, whose definition depends on

the data characteristics and their processing methods. Likewise, the disc-integrated measurements describe line parameters with respect to a continuum reference that is hardly identified in the solar and stellar spectra adjacent to the Ca II H & K lines, because of the presence of many absorption lines. Unfortunately, the various observations that are available in the literature have often been obtained with diverse instruments and methodologies, which renders their comparative analysis inconclusive.

We aim to contribute to a better knowledge of the Ca II H & K emissions, in particular of the relationship between Ca II K emission and magnetic field strength. As a first step, here we investigate the dependence of the Ca II K line data on different ambient conditions of the solar atmosphere due to different levels of magnetic flux, and characteristics of the observations, by using state-of-the-art data taken at solar disc center.

The paper is structured as follows. In Section 2 we describe the data analysed in our study and the methods used to process them. In Section 3 we present our results on the measured Ca II K emissions depending on the spectral and spatial resolution of the analysed observations. We discuss our results and summarise them by drawing our conclusions in Sections 4 and 5, respectively.

2. DATA AND METHODS

2.1. Observations

The data analysed in our study were acquired at the Swedish 1-m Solar Telescope (SST, [Scharmer 2006](#)) with the CRisp Imaging SPectropolarimeter (CRISP; [Scharmer et al. 2008](#)) and with the CHROMospheric Imaging Spectrometer (CHROMIS; [Scharmer 2017](#)) at the Fe I doublet lines at 6301.51–6302.50 Å (hereafter 6301–6302 Å) and the Ca II K line at 3933.67 Å (hereafter 3933 Å), respectively. In particular, we analysed three series of simultaneous full-Stokes Fe I and Stokes-I Ca II K observations acquired close to disc center by targeting a quiet-Sun area (QS) and an active region (AR), namely AR NOAA 12585. The CRISP and CHROMIS data are characterized by an image scale of $\approx 0.060''/\text{pixel}$ and $0.039''/\text{pixel}$, and a spectral resolution of about 60 mÅ and 120 mÅ, respectively, over a Field-of-View (FoV) of about $1' \times 1'$.

The QS data were acquired on 25 May 2017 from 08:06 to 11:16 UT at $\mu=0.99$, by targeting a region with patches of regular and irregular granulation, hereafter referred to as quiet-Sun granulation (QG) and quiet-Sun magnetized granulation (QM), respectively. The QS data consists of several scans of full-Stokes Fe I and Stokes-I Ca II K measurements. The Fe I line data were

taken sequentially at 9 spectral positions around the Fe I 6301 Å line centre, at 6 spectral positions around the Fe I 6302 Å line centre, and at -0.26 Å from the Fe I 6302 Å line centre for the continuum, by referring to rest-frame line centres. The Ca II K data were taken at 41 equally spaced positions in the range $[-1.30, +1.30]$ Å relative to the line centre and at 4000 Å for the reference continuum measurement. The cadence was 19.6 s and 13.6 s, for Fe I and Ca II K respectively.

The AR data were acquired on 5 September 2016 from 09:48 to 10:07 UT at $\mu=0.99$, by targeting a sunspot (SP) with umbral (UM) and penumbral (PE) regions and a neighbouring area (NA) with plages (PL) and several pores (PO), respectively. Similarly to the QS set, the AR data include several series of full-Stokes Fe I measurements and Stokes-I Ca II K data. Here the Fe I doublet lines were sampled as described above for the QS observations, while the Ca II K line measurements were obtained at the following 21 spectral positions: $[-1.4, -0.78, -0.70, -0.63, -0.55, -0.47, -0.39, -0.23, -0.16, -0.08, 0., +0.08, +0.16, +0.23, +0.39, +0.47, +0.55, +0.63, +1.25]$ Å relative to line center, i.e. on a slightly smaller spectral range than that used for the QS data, and at 4000 Å as the reference continuum. The Fe I and Ca II K datasets were taken at cadence of 32 and 14 s, respectively.

The data analysed in our study were extracted from all the observations available for the QS, NA, and SP regions, as the best frames among the 20 non consecutive observations of each solar target that are characterized by the highest contrast for best seeing during their acquisition.

The QS, NA, and SP observations have been previously studied by [Bose et al. \(2019\)](#), [Murabito et al. \(2021\)](#), and [Esteban Pozuelo et al. \(2019\)](#), respectively.

2.2. Data reduction

The data analysed in our study were reduced by using the CRISPRED (?) and CHROMISRED ([Löfdahl et al. 2021](#)) pipelines for CRISP and CHROMIS data, respectively. The processing consists of several steps, including among others application of bias and flat-field response of the detectors, compensation for spatial variation in the spectral instrumental response, for optics aberrations, and for atmospheric turbulence with the Multi-Object Multi-Frame Blind Deconvolution (MOMFBD, [Van Noort et al. 2005](#); [Löfdahl 2002](#)) image restoration. The latter step compensates for residual seeing degradation over the FoV unaccounted for by the adaptive optic system of the SST.

The data produced by the above pipelines were further processed as follows. Firstly, they were derotated

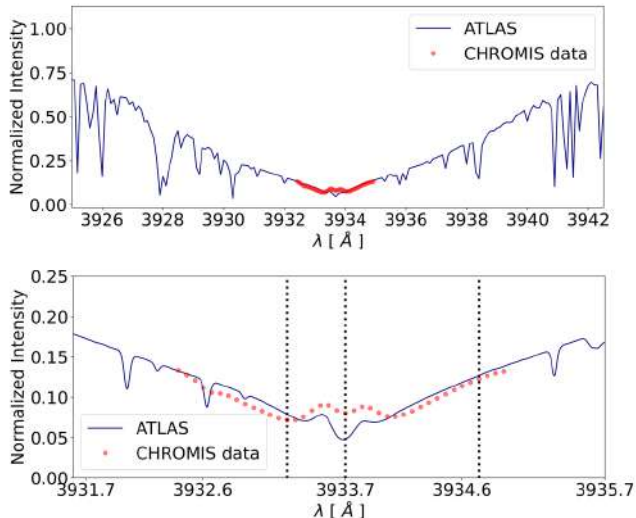


Figure 1. Examples of CHROMIS spectral sampling (red dots) of the Ca II K line 3933 Å. The measurements refer to a QS region and are normalized to the data at the reference continuum (not shown). Overplotted are disc center atlas measurements (blue solid line) from Delbouille et al. (1973). Vertical dotted lines mark the spectral samplings of the Ca II K observations shown in Fig. 2.

to account for diurnal field rotation. Then we aligned the CRISP and CHROMIS data and reduced them to the same pixel scale, by using as reference the frames acquired at the Fe I 6302 Å Stokes-I line continuum and Ca II K continuum at 4000 Å, which both originate in the low photosphere. In particular, we scaled up the CRISP data to the pixel scale of the CHROMIS data. This was done to maintain the original resolution of the Ca II K observations. Then, we rotated the CRISP images and trimmed them to match the FoV of the corresponding CHROMIS images. We used a cross-correlation technique to apply vertical and horizontal image shifts that result in a close match at sub-pixel accuracy. The above processing led to images that cover a region of about $50'' \times 40''$ for each target, with images having slightly different dimension of 1369×1066 , 1367×1004 , and 1403×1067 pixels² for the QS, NA, and SP datasets, respectively.

Figure 1 shows examples of the spectral-line profiles extracted from the data obtained from the processing described above. In particular, we show the sampling of Ca II K 3933 Å line resulting from spatial averaging of the data over the whole FoV of the QS set (red dots), depicted on the full spectra (solid line) from the disc-center atlas measurements from Delbouille et al. (1973)¹

for the sake of clarity. The data are normalized to the intensity of the reference continuum. We note that the spatially averaged Ca II K spectra are slightly higher for QS than the reference. This could be due to the analysed FoV.

Figure 1 makes it clear that the available Ca II K data only probe the Ca II K line centre with its typical double reversal and the innermost part of the line wings, but they do not sample the extended Ca II K line wings away from line centre that sample the deeper layers of the photosphere.

To account for these characteristics of the data we applied the following processing steps. First we performed the absolute wavelength and intensity calibration of the Ca II K observations. Due to the different shape of the profiles measured in the QS regions with respect to the ones measured in NA and SP areas² we used, as reference, the solar disc center atlas data by Delbouille et al. (1973) for the QS observations, and the sunspot umbral spectra from Wallace et al. (2005)³ for the NA and SP observations. Then, we extrapolated the analysed data to cover a wider spectral range than the one of the measured values, by using the atlas measurements at several spectral positions in the line wings as a reference. In particular, we assumed that the values extrapolated for the measured series follow the ones in the atlas at the following spectral positions [3916.9, 3924.0, 3929.6, 3932.4, 3935.0, 3939.5, 3942.1, 3949.3] Å for the QS observations, and at the following spectral positions [3924.0, 3929.6, 3932.4, 3935.0, 3939.5, 3942.1, 3949.3] Å for the NA and SP observations. It is worth noting that these positions were selected after several tests and trials aimed at optimizing the results obtained, while the slightly different spectral positions considered for the QS and other sets derive from the fact that the measurements of the atlas umbral spectra are only available for wavelengths larger than 3920.5 Å.

We used results from linear interpolations between pairs of the above reference positions to reconstruct values of an extrapolated line profile that mimic the behaviour of emission in the Ca II K line wings. However, we note that the data obtained by combining the measured and extrapolated values simulate high resolution spectral observations of the Ca II K line centre and low resolution spectral observations of line wings, the latter without accounting for the many lines that populate the spectra adjacent to the Ca II K line centre. We further

² The different shape is mostly in terms of the line width close to the line centre.

³ Available at <https://nispdata.nso.edu/ftp/pub/atlas/spot4atl/>

¹ Available at the BASS2000 Archive. <https://bass2000.obspm.fr>

consider this limitation of the data obtained from our processing in the following.

Finally, we applied spectral and spatial degradation to the data obtained from the previous processing steps, by convolving them with Gaussian kernel functions of varying width, in order to investigate the effect of spectral bandwidth and spatial resolution of the data on Ca II K observations and line measurements of various solar features. In particular, we convolved the CHROMIS observations, which were taken with a 0.12 Å spectral bandwidth, with 1D Gaussian functions having full-width-half-maximum (FWHM) of [0.2, 0.3, 0.4, 0.5, 0.6, 0.7, 1.0, 1.8, 2.5, 3.0, 5.0, 10.0] Å. These spectral widths (hereafter referred to as bandwidths and spectral degradations) match the bandwidths of most of the existing series of full-disc solar observations at the Ca II K (see e.g. Tables 1 and 2 in [Chatzistergos et al. 2022](#)). Moreover, we convolved the original data (with a spatial sampling of 0.039"/pixel) with a spatial 2D Gaussian kernel with FWHM of [0.18, 0.3, 1.0]". This spatial degradation was to represent the spatial resolution of the photospheric and chromospheric observations acquired with the SUNRISE's Imaging Magnetograph eXperiment (SUNRISE/IMaX, [Solanki et al. 2010](#); [Barthol et al. 2011](#); [Martínez Pillet et al. 2011](#); [Solanki et al. 2017](#)), Hinode's Solar Optical Telescope (Hinode/SOT, [Tsuneta et al. 2008](#); [Ichimoto et al. 2008](#)), and SDO's Helioseismic Magnetic Imager (SDO/HMI, [Pesnell et al. 2012](#); [Scherrer et al. 2012](#); [Schou et al. 2012](#)), respectively. We note that at present, the data from the above instruments are the most widely employed for studies of the photosphere and chromosphere. In addition, we also investigated the full-disc solar observations produced with a moderate spatial resolution resulting from a pixel scale larger than 2"/pixel. As mentioned above, these observations have been regularly obtained at several observatories since the beginning of the 20th century. We note that the instance of these observations is interesting in light of the role they play in connecting series of historical and modern full-disc solar Ca II K line observations ([Chatzistergos et al. 2022](#)). In this case we convolved the original CHROMIS data with a spatial 2D Gaussian kernel having FWHM of 4".

On both the original observations and data obtained from the above processing (i.e., the degraded data), we then evaluated two observable parameters of the Ca II K line that are widely employed for the monitoring of the chromosphere on the Sun and late-type stars. In particular, following, e.g., [Scargle et al. \(2013\)](#); [Björge et al. \(2018\)](#); [Dineva et al. \(2022\)](#), we estimated the K_3 intensity in Ca II K line core and the emission index equivalent width in 1 Å band centered on the line pro-

file (hereafter referred to as *EMDX*). Indeed, among the various Ca II K line parameters employed in the literature, K_3 and *EMDX* are the ones most sensitive to changes of the Ca II K line profile. We computed K_3 by measuring the intensity at 3933.67 Å, and *EMDX* by integrating the data with the five-point Newton-Cotes integration formula of the *int.tabulated* function in the *Interactive Data Language (IDL)*.

3. RESULTS

Figure 2 shows examples of the observations analysed in our study. In particular, we show the data taken at the Fe I 6302 Å line continuum (panels A–C), in the Ca II K line core (panels D–F), at roughly the secondary minimum K_{1V} in the violet wing of the Ca II K line (panels G–I), and in the red wing of the line at +1.05 Å from the line core (panels J–L), for the QS (left column panels), NA (middle column panels), and SP (right column panels) regions. We show the observations of the same solar features at the above diverse positions along the Ca II K line in order to highlight their different appearances as is in the case of the data of some existing series of Ca II K solar observations, e.g., the set of the Meudon Observatory that includes data at the centre and blue wing of the Ca II K line.

The photospheric Fe I data of the three observed regions show the regular granulation pattern in QS areas (panel A), elongated granules around the pores (panels B) and other larger scale features, such as the umbra and penumbra (panel C) in the SP target including bright umbral dots and dark and bright filaments, respectively. The Ca II K line core images display the chromosphere above the same areas, consisting of thin bright and dark fibrils everywhere, except in the umbra and inner part of the penumbra, and of several localised bright features (panels D–F). On the other hand, the data taken at the K_{1V} and in the red wing of the Ca II K line display disc features typical of the upper photosphere and temperature minimum, namely the reversed granulation pattern and the bright features in the intergranular lanes that are due to magnetic field concentrations and/or acoustic grains (panels G, J). These patterns are more evident in the red wing observations. Umbral regions are dark in all Ca II K observations, while in line core and line wing data penumbral areas are only partially so (panels F, I, L). We note extended brightenings may also appear in the umbral regions (in the chromosphere) due to umbral flashes. The pores are dark in line wing observations (panels H–K), while line core data display a small-scale (transient) brightening at higher atmospheric heights above them (panel E). All the Ca II K images show brightness patterns due to

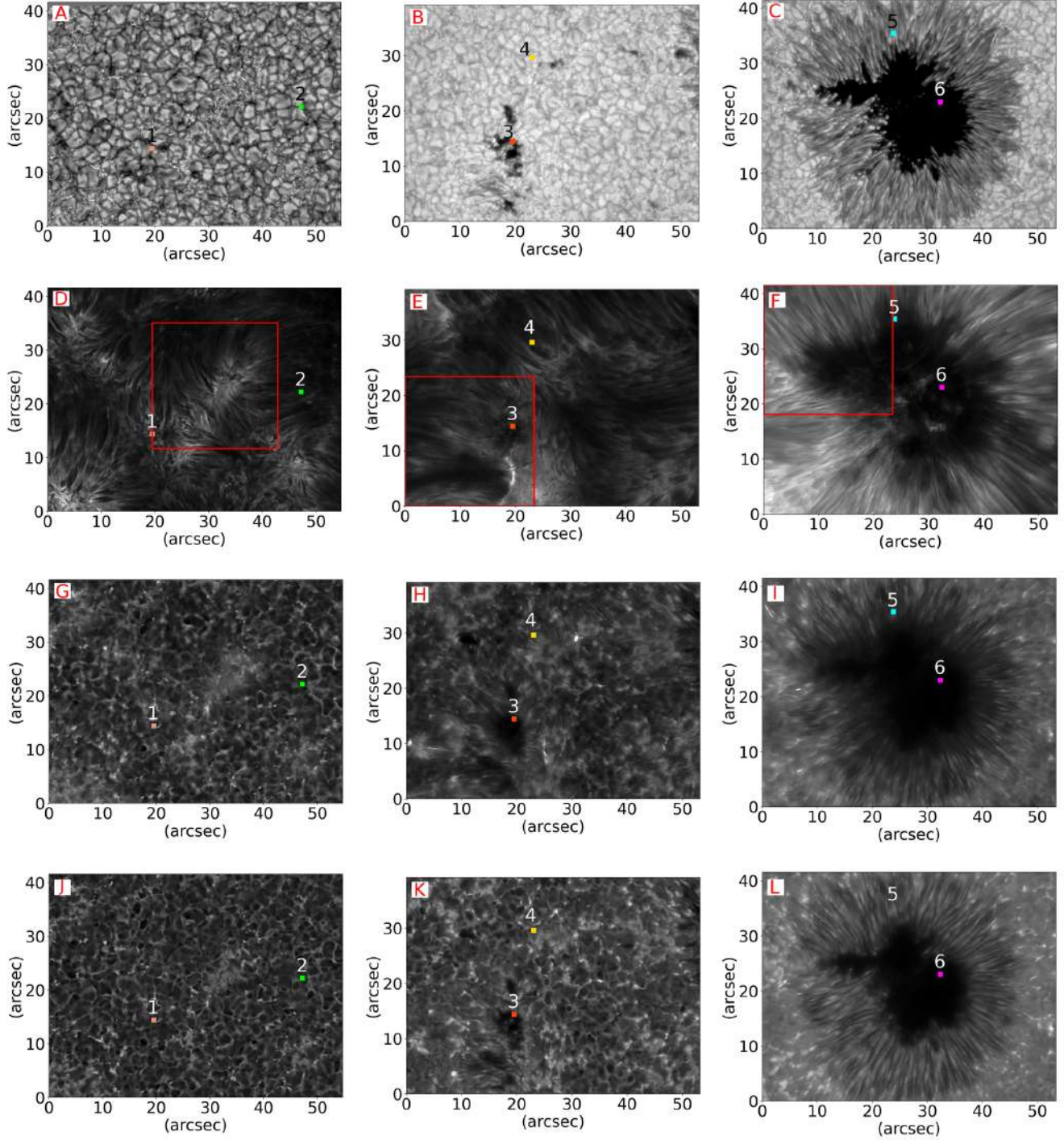


Figure 2. CRISP FeI 6302 Å continuum images (panels A–C) and CHROMIS Ca II K 3933 Å images in the line core (panels D–F), at -0.42 Å from the line core at roughly K_{1V} (panels G–I), and at $+1.05$ Å in the red wing (panels J–L) of the three regions analysed in our study, referring to a quiet Sun area (left column panels), an active region with plages and several pores (middle column panels), and a sunspot with umbra and penumbra (right column panels). After the image processing described in Sect. 2.2, the CRISP and CHROMIS observations are shown here with same dimension and pixel scale, which in the original data are in favour of the CHROMIS observations and is maintained here. Each observation is shown using the intensity interval that enhances the visibility of the solar features therein. The small coloured boxes show the six 20×20 pixels wide areas randomly selected in the observations to represent the solar features analysed in our study in the ambient to which they belong. The boxes are shown in all panels to make comparisons easier. The red boxes on line core observations mark the regions shown in Figs. 5, 7, and in Appendix B.

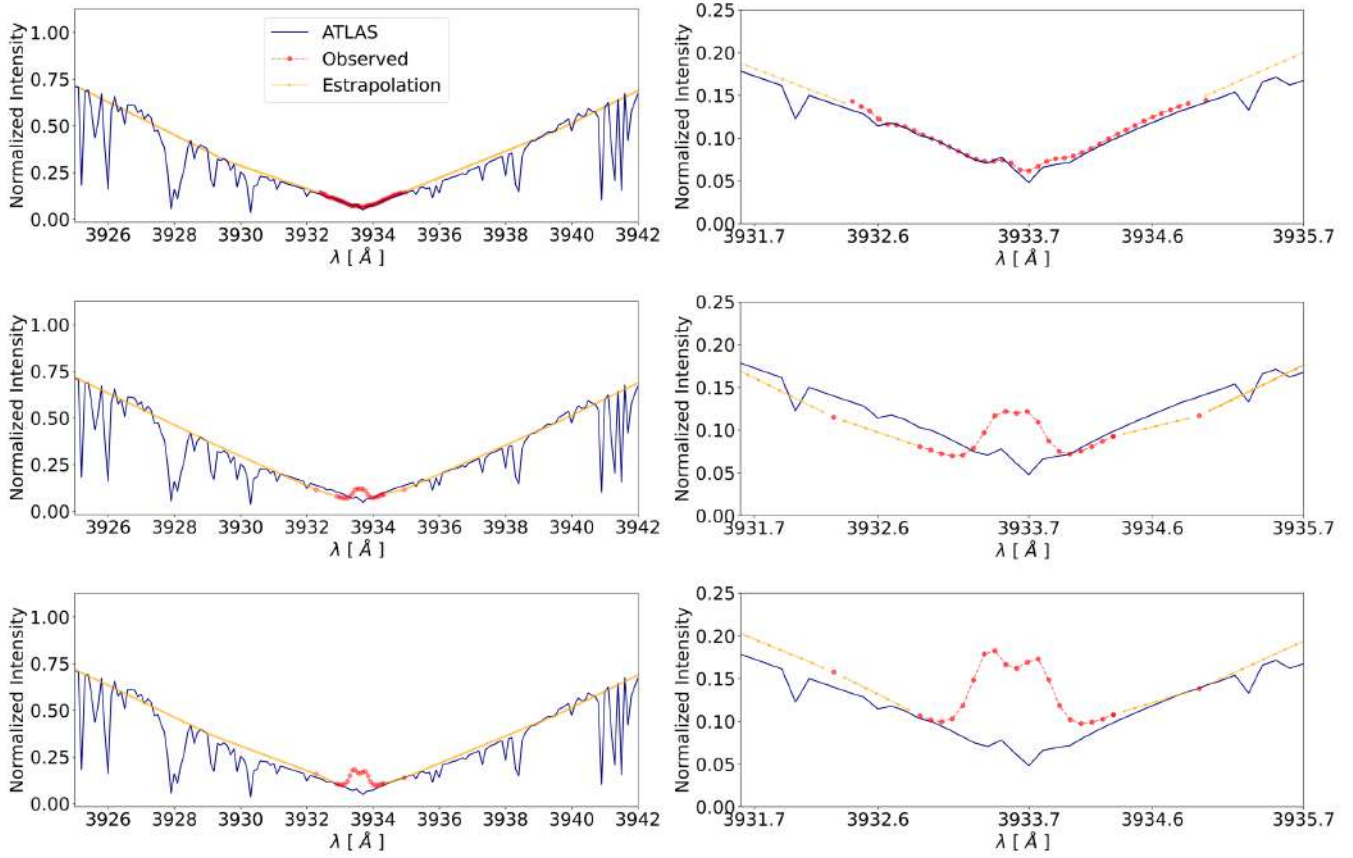


Figure 3. Examples of Ca II K line profiles analysed in our study. These were obtained by averaging data in sub-arrays representative of quiet areas in the studied QS (top panels), NA (middle panels), and SP (bottom panels) regions. The values are normalized to the data at the reference continuum at 4000 Å (not shown). The blue profile and red dots in each panel indicate the atlas data from [Delbouille et al. \(1973\)](#) and our observations, respectively. The yellow line describes the results from the data extrapolation based on atlas values.

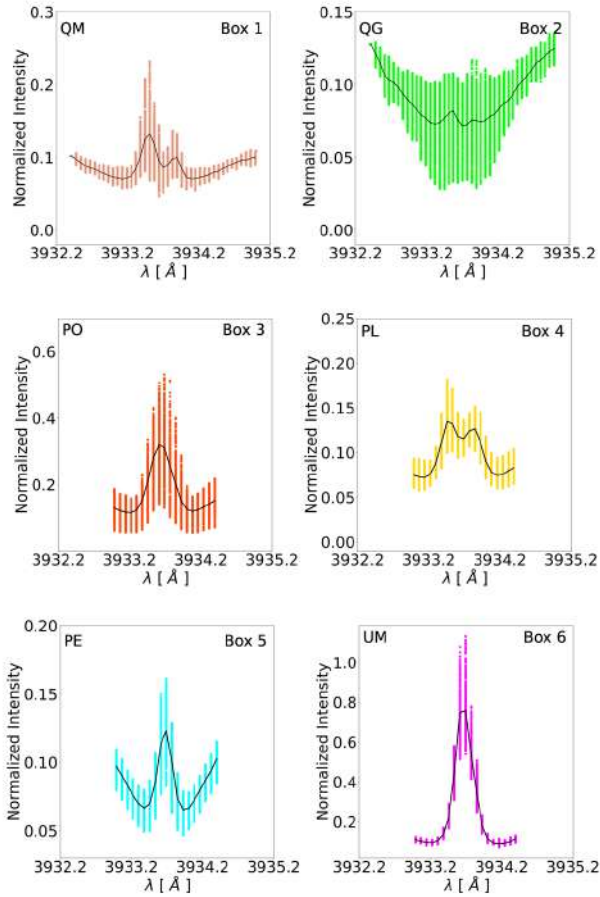


Figure 4. Examples of Ca II K line profiles analysed in our study. These were obtained from the 20×20 pixels wide areas marked with numbered and coloured boxes in Fig. 2. Black solid lines show the mean profiles derived from the spatially-resolved data available at each observed spectral position. We recall that the QS region (top row panels), to which the QM and QG areas belong, was sampled over a slightly larger spectral range than the NA (middle row panels) and SP (bottom row panels) regions, where the PO, PL, PE and UM areas were selected.

granulation and associated with dark magnetic features. Most of the bright/dark fibrils in the core images seem to overlie the bright patches displayed by the wing images (panels D, G, J and panels E, H, K). The fibrils observed in the Ca II K line core data are only slightly curved.

It is worth noting that the diverse solar regions described above are characterized by rather different Ca II K line profiles and are only representatives of the regions sampled in these observations that could look different based on, e.g., other magnetic topology. In Fig. 3 we compare Ca II K line profiles obtained from spatial averaging of the Ca II K line data in quiet areas of the QS, NA, and SP regions, overplotted on the high-

resolution spectrum from the atlas of Delbouille et al. (1973). Similarly to the latter, all the profiles derived from the observations show the K_{1V} and K_{1R} secondary minima in the violet and red part of the spectrum, respectively, the reversed line centre K_3 , and the two K_{2V} and K_{2R} peaks, with K_{2V} stronger than K_{2R} as reported in the literature. The above line features are almost inappreciable on the top right panel of the figure resulted from the QS observations, but they increase significantly in the data from SP regions (bottom right panel). On the other hand, in the NA case the K_3 line centre, and the two K_{2V} and K_{2R} peaks are not visible (middle right panel).

We notice that the separation of the line peaks and their width in all the QS spatially-averaged observed profiles are close to the ones in the atlas profile. However, this is not the case for profiles extracted from individual pixels in the analysed observations. Figure 4 displays some examples of these profiles, from the 20×20 pixels wide areas marked with numbers and coloured boxes in the QS, NA, and SP observations of Fig. 2. For each area under investigation, we also show the line profile (black solid line) derived from averaging the data available at each spectral position of our spatially resolved observations.

The profiles in Fig. 4 show different characteristics: there are profiles with emission peaks significantly increased (QM box 1, top left panel) with respect to the ones in Fig. 3, as well as profiles with fuzzy K_{2V} and K_{2R} peaks and a reversed strength than reported in the literature (QG box 2, top right panel), and profiles lacking the K_3 minimum (PO box 3, middle left panel; PE box 5, bottom left panel; and UM box 6, bottom right panel).

We note that the profiles in Fig. 4 derive from the areas randomly selected to represent diverse solar features in the ambient to which they belong. Indeed, analysing slightly different areas in their surroundings, the obtained profiles often retain the characteristics of the individual profiles in Fig. 4, but this is not always the case. Besides, the mean profiles derived from other boxes nearby the ones in Fig. 2 can slightly differ from the average profiles in Fig. 4. This is particularly evident in results derived from QM and QG data. Some examples for these data are given in Appendix A.

3.1. Effect of spectral bandwidth

We wondered how the Ca II K observations and measured line profiles presented in the previous Section are affected by the characteristics of the instruments employed for Ca II K measurements, in particular their spectral bandwidth and spatial resolution. To an-

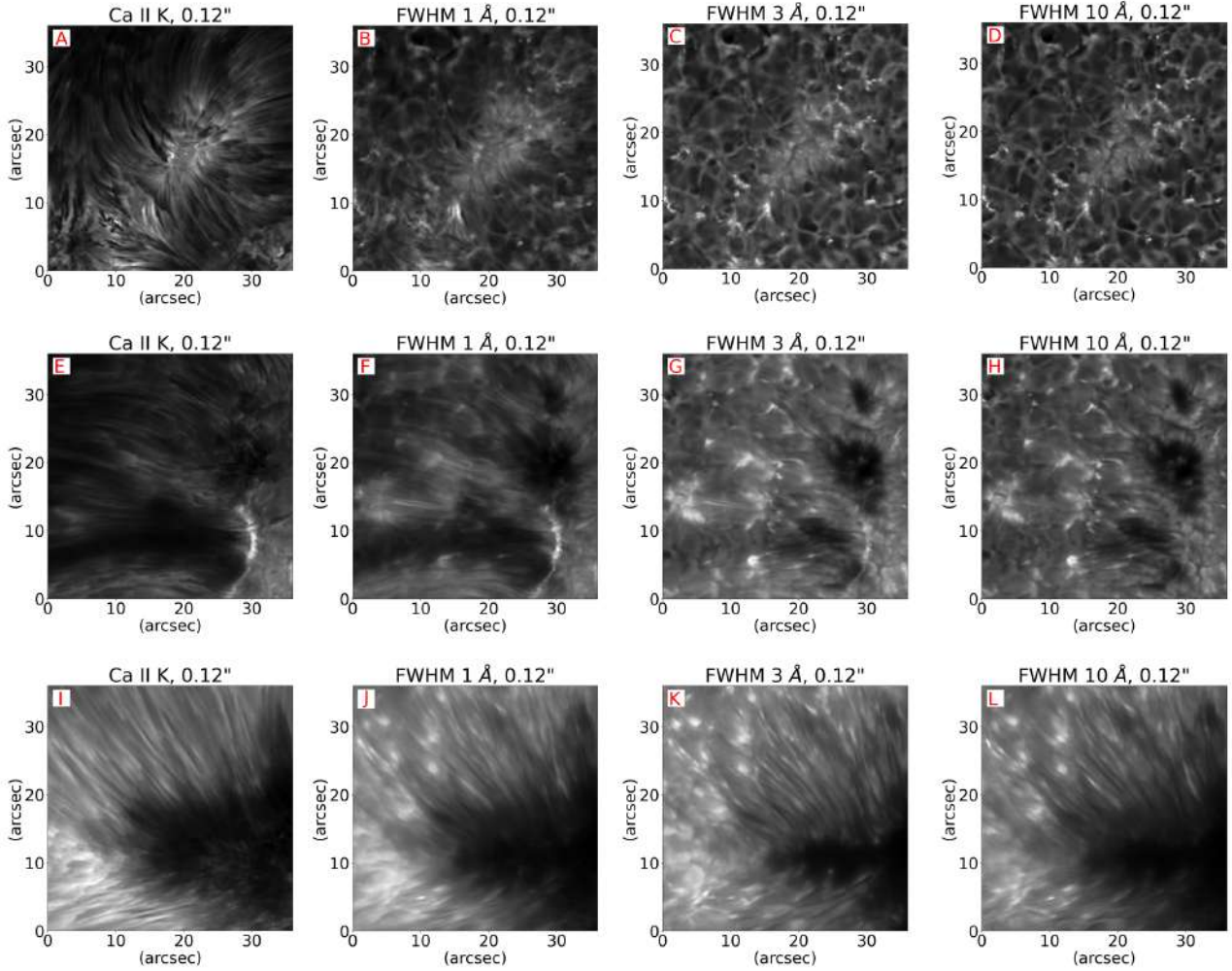


Figure 5. Examples of the observed (left column panels) and spectrally degraded (all other panels) images at the Ca II K line core of the three studied solar regions, namely a quiet Sun area (top row panels), a region with plages and several pores (middle row panels), and a sunspot with umbra and penumbra (bottom row panels), all observed close to disc center. For each target, from left to right we show original CHROMIS observations and data degraded with Gaussian kernels with FWHM of 1, 3, and 10 Å. Each image is shown using the intensity interval that enhances the visibility of the solar features therein.

answer the above question, in Fig. 5 we show an about $25 \times 25''$ FoV of the original CHROMIS observations at the Ca II K line centre for the three analysed solar regions (panels A, E, I) and corresponding data after their spectral degradation with kernels having FWHM of 1, 3, 10 Å (all other panels). The regions shown in Fig. 5 are the ones marked with red boxes in Fig. 2.

As expected, smearing the original data with a spectral kernel leads to mixing of photospheric and chromospheric emissions. The fibrils filling the original QS FoV (panel A) are faintly detectable with a spectral degradation of 0.6 Å (not shown) and almost no longer seen with 1 Å bandwidth (panel B), which allows PO and UM regions to manifest themselves with spatial scales and intensities (panels F, J) close to the ones displayed by the same features in images acquired with a spectral

degradation of 3–10 Å (panels G, K and panels H, L). Observations of the QS region with such bandwidths show the reversed granulation and dot-like bright features (panels C–D) seen in the original observations at the red wing of the Ca II K line (shown in Fig. 2, panel J).

Among the three regions studied here, the NA target is the one visually showing the largest change in its appearance with the various spectral degradation kernels. This applies, in particular, to data obtained with bandwidths up to 1 Å and those derived from bandwidths in the range [3,10] Å. Indeed, the former data show fibrils similar to penumbral filaments, while in the latter data bright granular elements appear around the pores. These granular features, which seem to be raised above the pores, are outlined by thin dark boundaries,

as reported in e.g. Lites et al. (2004) from a study of SST photospheric data. The same features also resemble the patterns attributed to sea-serpent magnetic configurations in e.g. Murabito et al. (2021). We also notice that the panels in Fig. 5, illustrating spectrally degraded data, show brightness patterns with similar position and extension in QS observations (panels B–D), and partly so in the SP data (panels J–L). However, the average Ca II K brightening of disc features in the above degraded images is always lower than in original CHROMIS observations. We also note that degrading the observations with larger kernels leads to appearance of smaller scale structures and finer details (panels D, H, L), and reversed granulation pattern (panels C–D).

The above effect of spectral degradation of the data is even more evident when considering the Ca II K line profiles. In Fig. 6 we show line profiles extracted from the original and spectrally degraded observations of the various targets in Fig. 5. We report spatially averaged profiles computed over the regions marked with numbers and coloured boxes in Fig. 2.

Figure 6 shows that a spectral degradation of the order of 10 Å results in an increase of the K_3 intensity of the Ca II K line core, and of the intensity all along the line profile, in all the areas except in the UM one. On the other hand, a spectral degradation of only 2.5 Å results in an increase of the K_3 intensity in QM and QG areas, being more evident in the latter case, and a decrease of the same quantity in all the other targets. Noteworthy, spectral bandwidths from 0.7 Å to 2.5 Å have similar effects on the line profiles derived from the PO and PL areas.

Figure 6 also shows that the features of the Ca II K line typical of each studied areas disappear completely in observations characterized by a bandwidth of 1.8 Å. It is worth noting that this spectral bandwidth is lower than the ones used by most sites currently performing observations in the Ca II K line with optical filters, but higher than all the ones of spectroheliograph data (see Chatzistergos et al. 2022).

We note that the various panels in Fig. 6 also include shaded areas, which cover the range of values measured over each analysed region. These shaded areas manifest the large heterogeneity of the Ca II K line profiles in the studied observations when considered at the spatial resolution of the CHROMIS observations. This heterogeneity is particularly evident in the QS data, that seem to be especially affected by intensity oscillations due to hydrodynamic pressure modes (p-modes, Leighton 1960), and very noticeable in the line wings, where small changes in wavelength due to p-modes lead to large variations in intensity. On the other hand, intensity fluctuations are

also evident in the profiles derived from the NA areas, while they are not appreciable in the profiles obtained from the SP field. The intensity fluctuations in both these regions are most likely attributable to magneto-hydro-dynamical oscillations (MHD-modes, e.g. Spruit 1982) and to small scale transient brightening from magnetic reconnection events.

Overall, the results presented above suggest that the effect of spectral bandwidth on Ca II K line profiles depends on both the employed bandwidth and observed solar region.

3.2. Effect of spatial resolution

We then considered the impact of spatial degradation on our data. As an example, in Fig. 7 we show data derived from spatial degradation of the original observations of the QS region, under the diverse spectral degradations analysed above. For the sake of comparison, we also show the original CHROMIS observations, characterized by a spatial resolution of 0.078". More examples for the QS, NA, and SP regions are given in Appendix B and presented in the following. For all these examples, we considered the spatial resolution of the SUNRISE/IMaX, Hinode/SOT, and SDO/HMI observations acquired with a pixel scale of 0.09, 0.15, and 0.5"/pixel, respectively. Moreover, we considered the case of the synoptic full-disc observations characterized by a moderate pixel scale of 2"/pixel, as in the data acquired at e.g. the Rome Observatory. Results for the latter case are also reported in Appendix B.

For the data representative of all the above pixel scales, we considered spectral degradations resulting from the application of Gaussian kernels with FWHM of 1, 3, and 10 Å to the original CHROMIS data characterised by a 0.12 Å spectral resolution. The above FWHM values are distinctive of the bandwidth of optical filters employed for modern observations in the Ca II K line, at e.g. the Rome, Kanzelhöhe, and San Fernando Observatories, respectively.

From the data in Fig. 7, we notice that the spatial degradation impacts almost equally the data characterised by a spatial resolution better than 0.3". Besides, we observe that the appearance of the data is barely affected by employed spectral bandwidths in the range [1,10] Å. This also applies to data degraded to the 4" spatial resolution typical of full-disc observations, which show the main features of the observed regions seen in the higher resolution data preserved on larger spatial scales, and less details at the small scales. These findings are in agreement with the results reported by ? concerning reconstructions of irradiance variations and unsigned magnetograms derived

from Ca II K observations, which both resulted to be only slightly sensitive to the bandwidth of the analysed observations in the range $[0.09, 9]$ Å and to the data spatial resolution in the range of $\sim [2, 11]''$.

As mentioned above, more examples of solar regions data at the original resolution of the CHROMIS observations and derived from the various degradation kernels applied to them are given in Appendix B. In particular, we show examples of the QS region observed in the red wing of the Ca II K line at $+1.05$ Å from line core and of the NA and SP areas observed at the Ca II K line core. From these additional examples we note that regardless of the spatial and spectral degradation applied to the data, the QS target shows different characteristics when observed in the Ca II K line core and in the red wing of the Ca II K line, but the latter resemble observations at the K_{IV}. On the other hand, we notice that the granular bright features surrounding the pores in the NA region observed at the Ca II K line core with the $0.078''$ original spatial resolution of the CHROMIS data, and with bandwidths in the range $[3, 10]$ Å, are retained in the data degraded to a spatial resolution up to $0.3''$, while they form unresolved larger scale bright features in the data characterised by a spatial resolution of $1''$. We also note that the arc-shaped feature with largest intensity gradient seen in the original NA observations is visible in all the data derived from spatial degradation up to $1''$ and spectral bandwidths up to 3 Å, although with lower intensity. However, in addition to this arc-shaped feature, spatial and spectral degradations bring out in the observed field several dot-like and small-scale bright structures unseen in the original data. This also applies to observations of the SP target at the Ca II K line core. In these data we notice that the appearance of the umbral and penumbral regions is only barely affected by a spatial degradation up to $1''$ and spectral degradation up to 1 Å. Indeed, the umbral and penumbral areas are almost unaffected by the spatial degradation applied to the data, while their extension slightly decreases in the data degraded with spectral kernels larger than 1 Å.

In Appendix B we also show examples of the QS, NA, and SP regions observed at the Ca II K line core and reported in Fig. 2, as returned when degraded to a spatial resolution of $4''$ and to spectral bandwidths in the range $[0.12, 10]$ Å. We notice that these data show unresolved bright patterns that are rather unaffected by the spectral degradation applied to the data. We also report a marginal decrease of the umbral area for data with spectral degradation larger than 1 Å. It is worth noting that the umbral region in the degraded data shows almost same extension than the same region in the full resolution photospheric CRISP observations

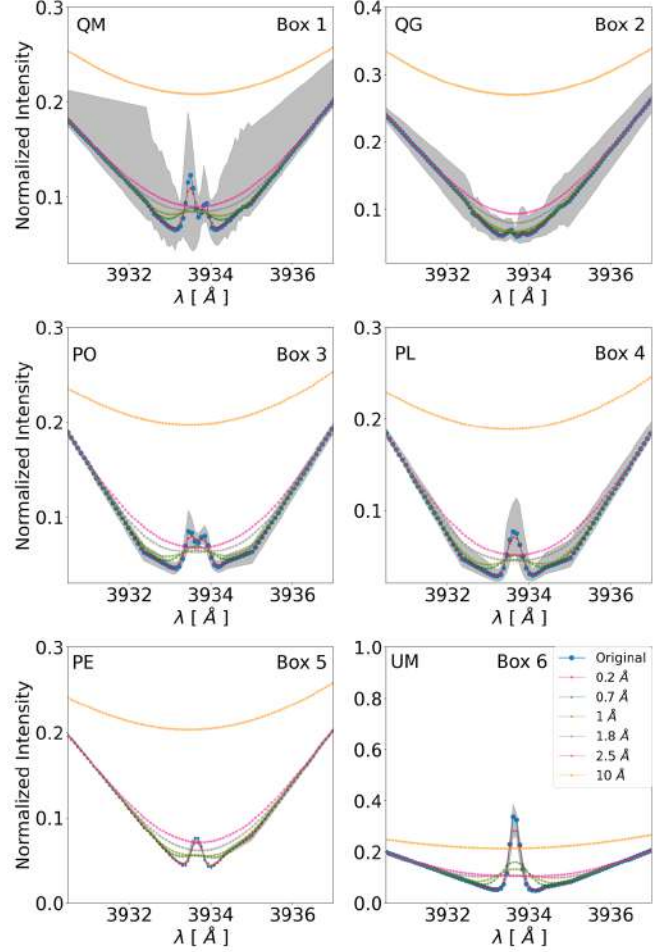


Figure 6. Ca II K line profiles derived from data averaging over the areas marked with numbers and coloured boxes in Fig. 2. The diverse profiles are color-coded depending on the degradation applied to the original data and according to the legend in the bottom-right panel. From top to bottom we show the profiles for the selected areas in the QS (top row panels), NA (middle row panels), and SP (bottom row panels) observations, respectively. The profiles are normalized to the continuum intensity at 4000 Å (not shown). The grey shaded areas cover the range of values measured in the analysed regions at each spectral position.

and chromospheric CHROMIS data at the red wing of the Ca II K line.

3.3. Focus on line parameters

Figure 8 describes the impact of the spectral degradation on the K_3 and $EMDX$ parameters derived from the diverse solar data considered in our study. In particular, we display the variation of the K_3 (left panels) and $EMDX$ (right panels) parameters depending on the spectral kernel applied to the line profiles averaged over the whole QS region and over the QM (box 1) and QG (box 2) areas selected therein (top panels), as well as over the PO (box 3) and PL (box 4) areas in the NA re-

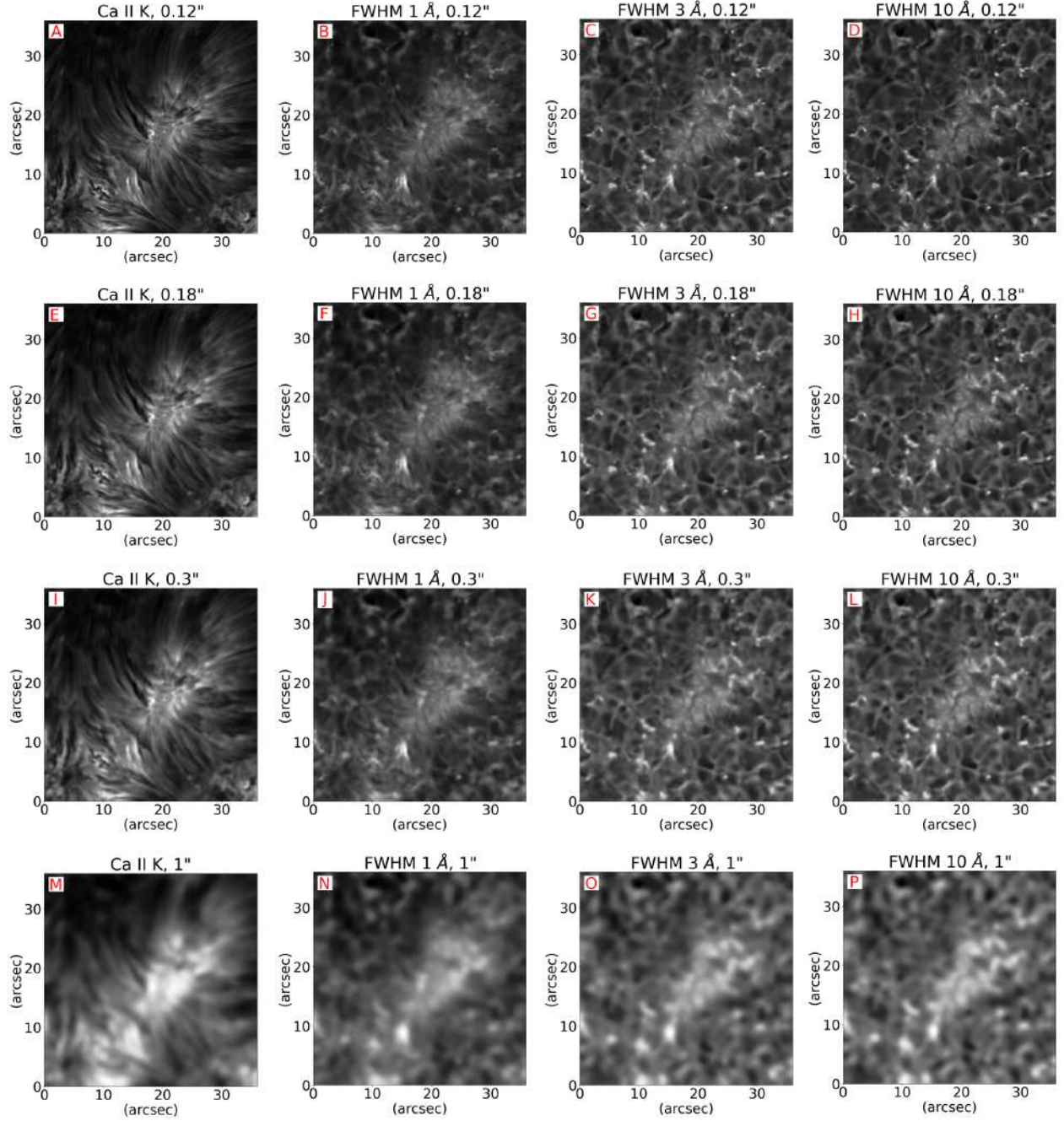


Figure 7. Examples of the original (panel A) and degraded (all other panels) images at the Ca II K line core of the QS region, to account for the diverse bandwidths and spatial resolutions of the most prominent series of available Ca II K observations. Each row shows examples of data characterized by a given pixel scale and by different bandwidths. From top to bottom, we show data at the original pixel scale of the CHROMIS observations (panels A–D) and degraded to a spatial resolution of 0.18'' (panels E–H), 0.3'' (panels I–L), and 1.0'' (panels M–P), as is in the case of the SUNRISE/IMaX, Hinode/SOT, and SDO/HMI observations, respectively. For each of these observations, from left to right we show the data at the spectral resolution of the CHROMIS observations of 0.12 Å, and spectrally degraded with Gaussian kernels with FWHM of 1, 3, and 10 Å. Each image is shown using the intensity interval that enhances the visibility of the solar features therein.

gion (middle panels), and the PE (box 5) and UM (box 6) areas in the SP target (bottom panels). We also report the dependence of the same parameters estimated by using the respective reference atlas data.

Figure 8 (top panels) shows that the K_3 and $EMDX$ parameters derived from the QS and QG (QM) degraded data increase gradually for spectral bandwidths larger than 1 Å (2 Å) and are almost unaltered in observations with bandwidths in the range [0.12,1.0] Å ([0.12,2.0] Å). Therefore the sensitivity to spectral degradation of both parameters obtained from QS and QG areas is slightly different from the one derived from the QM region. We notice that the trend derived from the whole QS target reproduces the variation of the parameters derived from atlas measurements better than obtained from the other regions, except for a difference in the estimated values. The increase of the K_3 ($EMDX$) values is of the order of about 2 %/Å (1.5 %/Å) for the QS observations with spectral bandwidth larger than 1 Å.

We also studied the K_3 and $EMDX$ parameters in the profiles derived from the PO (box 3), PL (box 4), PE (box 5), and UM (box 6) observations. As shown in Fig. 8 (middle panels) the variation of the K_3 and $EMDX$ parameters derived from the PO and PL areas are close to each other for spectral bandwidth of about 0.2 Å and exhibit a similar behaviour for all larger bandwidths, with differences that tend to decrease for bandwidths larger than 1 Å. We also note that for spectral bandwidths in the range [0.12,10] Å, the results derived from the NA region (middle panels) are rather similar to those obtained from the QM area (top panels). The same applies to the findings from the PE region (bottom panels), but limited to spectral degradations in the range [1,10] Å. Besides, Fig. 8 (bottom panels) displays that for UM regions the values of the K_3 and $EMDX$ parameters estimated from the spectrally degraded data increase gradually for bandwidths larger than about 3 Å, while the values of both parameters decrease in observations with a spectral degradation in the range [0.12,2] Å. This decrease of the values of the K_3 and $EMDX$ parameters is of the order of 35 %/Å and 18 %/Å, respectively, while the increase of the parameters for the data with bandwidths in the range [3,10] Å is of the order of 1 %/Å. Similarly to results from the QS and QG regions, the parameters computed for the PE area are almost unaltered in observations with spectral bandwidth in the range [0.2,1.0] Å, while they increase gradually of about 1 %/Å for the data with bandwidths in the range [1,10] Å.

We notice that the K_3 and $EMDX$ parameters computed on each observed region vary with the spectral degradation applied to the data in a rather similar way.

Therefore, in the following we further consider the characteristics of the K_3 variation only.

We report that the best relation describing the changes of the K_3 parameter on the spectral bandwidth of the data is a polynomial function of the fifth order that is represented by the equation

$$K_3 = ax^5 + bx^4 + cx^3 + dx^2 + ex + f, \quad (1)$$

where x is the spectral bandwidth considered, expressed in Å. Table 1 summarizes the $a - f$ parameters for the various studied data.

We find that the fitted curves follow the data derived from the observations with minute deviations. Indeed, all the fits give mean standard deviation between original and fitted curves in the range $[1.8,15.4] \times 10^{-4}$, except for the UM data, which show a mean deviation of about 62×10^{-4} . However, we notice that the fitting of the UM data is slightly better represented by a polynomial function of the sixth order⁴, which results in an average deviation of about 26×10^{-4} . Note that we derived the mean deviation from the average difference between original and fitted values, and the 1σ uncertainty from the diagonal values of the covariance matrix of the optimal coefficients computed with the *scipy.optimize.curve_fit* function in the *Python* language.

We then considered the effect of the spatial degradation on the values of the K_3 parameter estimated for the various solar regions and spectral bandwidths considered in our study.

Figure 9 displays the variation of the K_3 parameter derived from the line profiles averaged over the whole QS region and selected QM and QG areas (top panel) therein, as well as over the PE and UM regions (bottom panel) of the SP target, by considering the CHROMIS data and those obtained from the various spectral and spatial kernels applied to them. Similarly to findings in Fig. 8, results from the PL and PO areas are close to the ones reported for the QM and UM regions, respectively, and are thus not shown.

Results in Fig. 9 suggest that the effect of the spatial degradation on K_3 values depends on the solar target. It is significant for the selected areas representative of the QM region (box 1) in the QS target, and of the PE (box 5) and UM (box 6) areas in the SP region. In particular, for observations of the QM, PE, and UM regions,

⁴ Described by the equation $K_3 = ax^6 + bx^5 + cx^4 + dx^3 + ex^2 + fx + g$, with the following coefficients: $a=(0.8 \pm 0.2)10^{-5}$, $b=(-0.02 \pm 0.3)10^{-4}$, $c=(0.01 \pm 0.2)10^{-3}$, $d=(-0.5 \pm 7)10^{-2}$, $e=(0.01 \pm 0.0009)10^{-2}$, $f=(-0.1 \pm 0.05)10^{-1}$, $g=(6.8 \pm 0.0008)10^{-1}$.

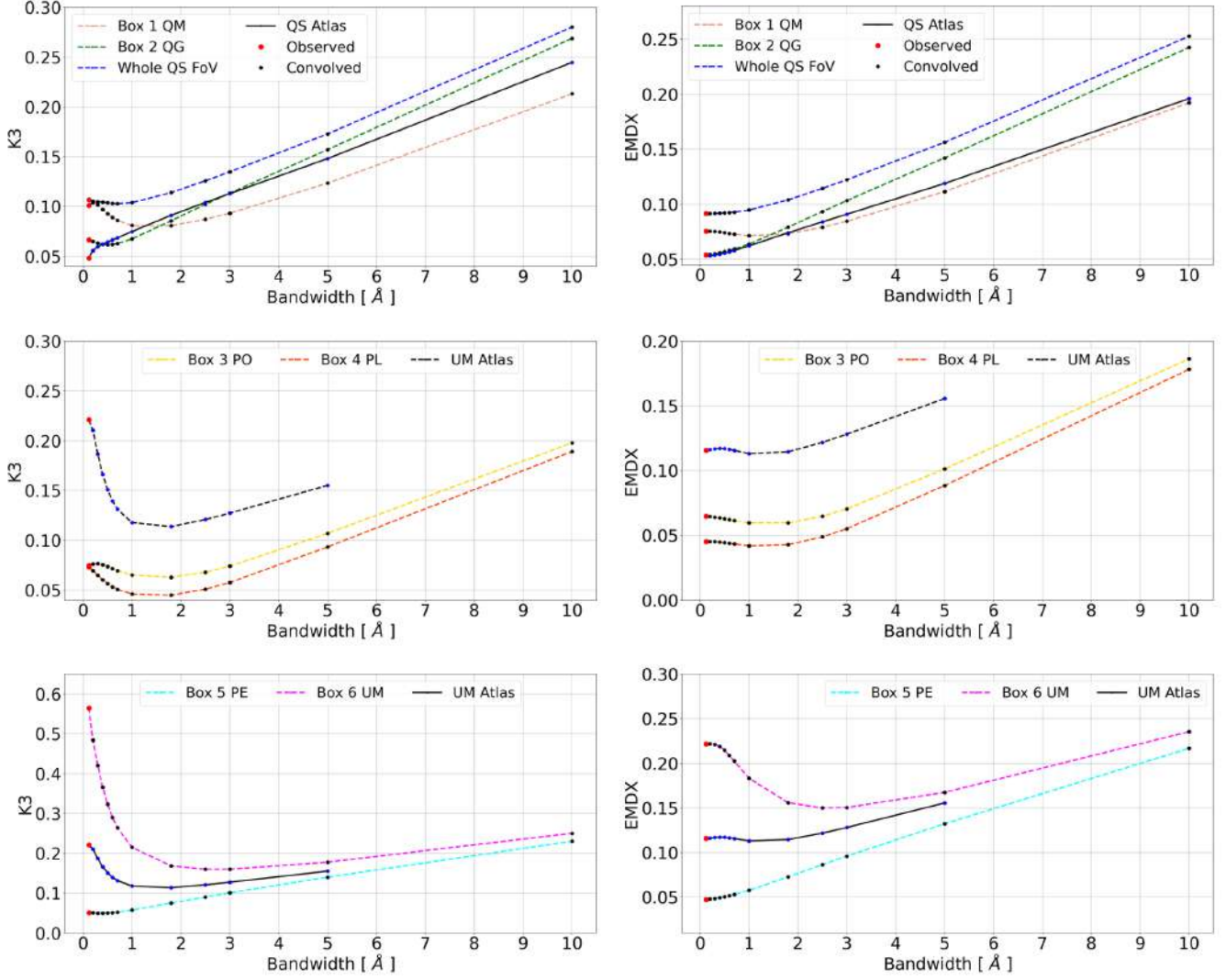


Figure 8. Dependence of the K_3 (left column panels) and $EMDX$ (right column panels) parameters estimated from the Ca II K line measurements on the QS region and on the QM and QG areas therein (top row panels), PO and PL areas in the NA target (middle row panels), and PE and UM areas selected in the SP observation (bottom row panel), depending on the spectral degradation applied to the analysed data. Overplotted to each panel is the variation of the parameter derived from the relevant atlas data (black solid line) after their spectral degradation with the various kernels used in our study. Find information about the atlas data in Sect. 2.2.

K_3 changes of about [2,30] %, -[5, 20] %, and -[15,40] % maximum when the data are degraded to observations with spatial resolution from $0.18''$ to $1''$, which represent the cases of the SUNRISE/IMaX and SDO/HMI observations, respectively. K_3 changes in QM, PE, and UM areas from about 5 %/ \AA to 20 %/ \AA , 15 %/ \AA to 30 %/ \AA , 0.1 %/ \AA to 30 %/ \AA minimum to maximum when considering data with a spectral degradation given by bandwidths in the range [2,10] \AA . For the QG and QS areas the spatial degradation affects only minutely the estimated value of the K_3 parameter.

4. DISCUSSION

The observations analysed in our study were compensated for residual effects of atmospheric turbulence, and calibrated with atlas measurements before their degradation to match the diverse spectral and spatial resolutions considered. However, they are not compensated for the stray-light contamination, which is estimated to be low and mostly to come from the SST instruments (Scharmer et al. 2019). Intensity values analysed in our study may thus suffer from incomplete compensation of stray-light, because the spectral intensity calibration applied to the data using the disc center atlas spectrum as reference does not remove all instrumental effects. Based on comparison between intensity values

Table 1. Results from K_3 parameter fitting.

Region	a	b	c	d	e	f	mean SD
	$[10^{-5}]$	$[10^{-4}]$	$[10^{-3}]$	$[10^{-2}]$	$[10^{-2}]$	$[10^{-1}]$	$[10^{-4}]$
QM	-3.5 ± 2.5	8.8 ± 4.9	-8.1 ± 2.9	3.5 ± 0.7	-6.2 ± 0.6	1.1 ± 0.01	6.8
QG	-9.5 ± 0.76	19 ± 1.4	-14 ± 0.8	4.3 ± 0.2	-3.4 ± 0.2	0.7 ± 0.004	2.0
QS	2.4 ± 2.9	-4 ± 5.5	1.5 ± 3.3	2.8 ± 0.7	-0.2 ± 0.7	1 ± 0.02	8.1
PE	-7.2 ± 0.7	15 ± 1.3	-10 ± 0.8	3.1 ± 0.2	-1.8 ± 0.2	0.5 ± 0.004	1.8
UM	-141 ± 22	294 ± 42	-209 ± 25	65 ± 5.8	-92 ± 5	6.5 ± 0.1	61.5
QS Atlas	5.7 ± 3.5	-11 ± 6.5	7.8 ± 3.9	-2.2 ± 0.9	4.6 ± 0.8	4.6 ± 0.2	9.2
UM Atlas	-136 ± 80	191.4 ± 86.7	-102.9 ± 31.7	26.7 ± 4.8	-32.7 ± 2.8	2.6 ± 0.05	15.4

NOTE—Columns are: solar region over which the relationship was studied, best fit parameters (a, b, c, d, e, f) with their 1σ uncertainties, and the mean standard deviation (SD) between original and curves of the fits. Find more details in Sect. 2.2 and Sect. 3.3.

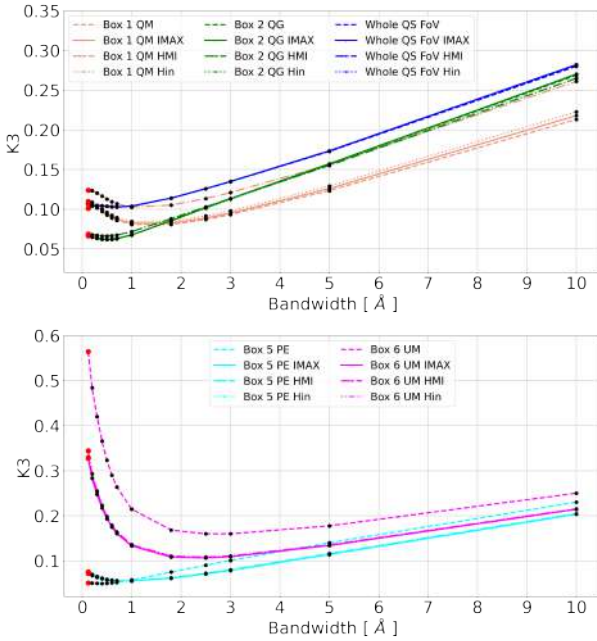


Figure 9. Dependence of the K_3 parameter estimated from the Ca II K line measurements on the QS, QG, and QM areas (top panel) and on the PE and UM regions (bottom panel), depending on the spectral and spatial degradation applied to the analysed data, representative of various observations. Find more details in Sects. 3.2 and 3.3.

measured in the QS target and in the atlas reference we expect compensation for stray-light to affect line core intensities reported from our study with an increase of their values of about 40 % and 80 % in QS and PO penumbral data, respectively. Moreover, we would like to emphasize that the observations and line intensities reported in this study might not be representative of all the similar solar and stellar data. Indeed, we highlight that they refer to the specific level of solar magnetism

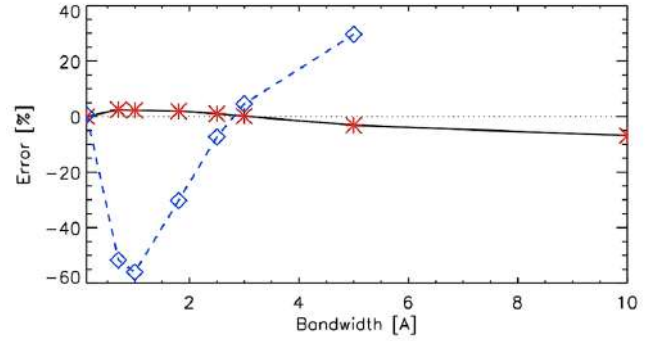


Figure 10. Error [%] in the K_3 values estimated from atlas data representative of QS region (solid black line, red star symbols), and NA and SP (dashed blue line, diamond blue symbols) regions, depending on the spectral degradation applied to the data. For the sake of clarity overplotted is the null error line (dotted line).

and solar activity framed by the observations analysed in our study.

In addition, we have reported results based on line profile data that combine measured values in the inner part of the line and extrapolated values in the line wings. As stated above, these data simulate low resolution spectral observations in the line wings and high resolution observations in the line core. In addition, the extrapolated values do not account for the many lines that populate the spectra adjacent to the Ca II K line core. We investigated the impact of the unaccounted line blending in the obtained results. To this end, we analysed atlas data and applied to these all the processing steps performed on the observations analysed in our study.

Figure 10 summarizes information about the error expected for our estimated values by missing the effect of line blending in the analysed data. We notice that this error can lead to either underestimating or overestimating the K_3 values depending on the observed region and

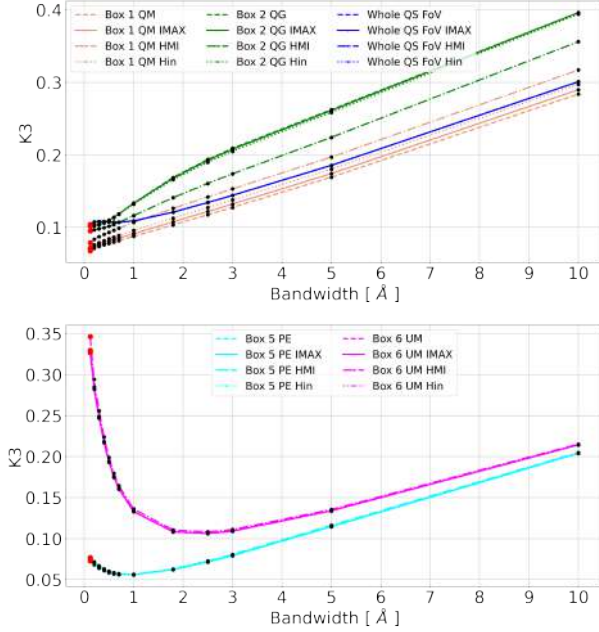


Figure 11. Dependence of the K_3 parameter estimated from the Ca II K line measurements on the QS, QG, and QM areas (top panel) and on the PE and UM regions (bottom panel), depending on the spectral and spatial degradation applied to the analysed data, representative of various observations. Here the reported values derive from average Ca II K line profiles computed pixelwise on spectrally and spatially degraded data. Find more details in Sect. 4.

bandwidth of the analysed data. In particular, for the QS and PL data, it leads to underestimate the K_3 parameter up to 2.5 % for data with 0.7 Å bandwidth, while there is an overestimation of the values for the data with a spectral degradation in the range [3,10] Å. In this case the error increases linearly up to about 7 %. On the other hand, for the PO and UM data represented by the corresponding atlas, the approximation applied in our study can lead to an overestimation of K_3 values up to 50 % for data with a bandwidth of 1 Å, and to an underestimation of the values for data with spectral widths in the range [3,5] Å. In this case the underestimation error increases linearly up to about 30 %. Note that the smaller range of bandwidths over which we can investigate the effect of line blending in UM atlas data derives from the fact that those measurements are available only for wavelengths larger than 3920.5 Å. Overall, the estimated errors suggest that the findings presented above shall be deemed to be indicative of the studied dependence and as an underestimation of its effects.

Furthermore, we have presented results from spatially-resolved data, both observations and line profiles, as well as from average profiles computed over small ar-

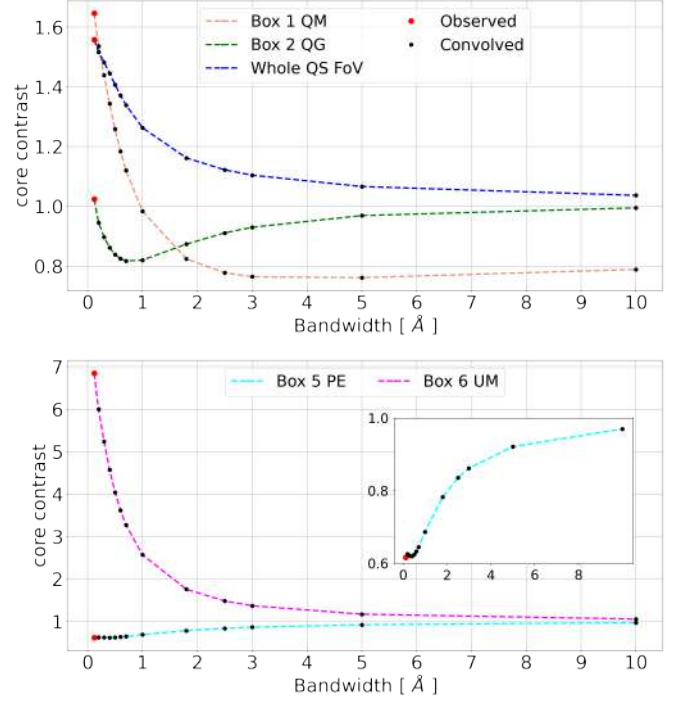


Figure 12. Dependence of the estimated line core intensity contrast on the spectral resolution of the analysed data, on the whole QS region and on the QM and QG areas therein (left panel), as well as on the PE and UM areas selected in the SP observations (right panel). See Sect. 4 for more details.

eas (20×20 pixels wide, i.e. covering a photospheric region of about $0.8 \times 0.8''$) selected to represent six solar features in the ambient to which they belong. We note that the latter data describe observations that are indeed characterized by a lower spatial resolution than that of the original CHROMIS measurements. This can explain the small dependence on the explored spatial degradations of most of the K_3 values reported in Fig. 9. We however acknowledge that those results may not represent findings from similar estimations based on different computational approaches to account for the data characteristics. In particular, we found that the dependence of K_3 values on the spectral and spatial degradation of the data slightly differ whether K_3 is estimated by maintaining the original resolution of the observations or by degrading it to the one of the selected small areas. The impact of the approach applied to estimate K_3 is however minute. In particular, Fig. 11 shows the variation of the K_3 parameter derived from data of the QS, QM, and QG regions (top panel), and of the PE and UM areas (bottom panel), by considering the original CHROMIS observations and the data obtained from the spectral and spatial kernels applied pixelwise

to them. The results in Fig. 11 suggest that the diverse approaches, namely considering the average profile of small areas or profiles derived pixelwise, affect the K_3 values obtained, but they only marginally impact the exact form of the relation describing the K_3 variation on data characteristics. Indeed, for the ranges of spectral and spatial degradations explored in our study, we found that this relationship is basically linear over the range $[2,10]$ Å for all the investigated regions.

Finally, in our study we considered K_3 to quantify the Ca II K brightening in the diverse image pixels and solar features in our data sets, but this quantity is also defined in the literature as line core intensity contrast C , where $C = I/I_{QS}$, and I and I_{QS} are the Stokes-I intensities at the Ca II K line core over each image pixel and mean QS intensity averaged over the entire FoV analysed, respectively; see e.g. Kahil et al. (2017).

In Fig. 12 we show the variation of the line core intensity contrast estimated on the whole QS region and on the several selected areas of Fig. 2. Firstly, we notice that the values and trends in Fig. 12 largely differ from the ones reported in Fig. 8 due to the diverse reference intensities employed to derive the quantities in the respective figures. Besides, Fig. 12 displays that the line core contrast decreases monotonically at the increase of the spectral degradation of the data for observations of the whole QS target and UM areas, while it shows a different variation on the selected areas of QS (QM box 1 and QG box 2) and of PE (box 5) regions. The decrease of the line core contrast in average QS and UM regions is particularly severe for bandwidths up to about 2.5 Å and of the order of 40 %/Å and 500 %/Å, respectively. Results from the selected QS area characterized by regular granulation (QG box 2) display a hook-like trend with the decrease of the estimated contrast up to a minimum for bandwidths up to about 1 Å and increase of the contrast for larger spectral widths. On the other hand, the contrast values derived from the PE area show a monotonic increase with the bandwidth, which is of the order of 50 %/Å for observations with bandwidth up to about 5 Å.

5. SUMMARY AND CONCLUSIONS

We investigated the variation of observations and line profile measurements at the Ca II K line depending on spectral bandwidth and spatial resolution of the data, and on ambient in the solar atmosphere. We used state-of-the-art observations of the solar photosphere and chromosphere obtained with the CRISP spectropolarimeter and CHROMIS spectrometer operating at the Swedish Solar Telescope. We studied three data sets that relate to very different conditions in the solar at-

mosphere, representative of a quiet Sun area, a region with plages and several small pores, and a large sunspot with umbra and penumbra.

Firstly, we noticed the large heterogeneity that characterize the Ca II K line profiles measured over the studied regions when considered at the full spectral and spatial resolution of the CHROMIS data. This heterogeneity is particularly evident in the data derived from the QS areas, which show intensity variations due to, e.g., p -modes oscillations. However, different and distinguishable elements of the Ca II K line profiles derived from the diverse studied regions are retained when the data are averaged over areas selected to represent the solar region to which they belong.

We then noticed that the effect of spectral degradation on Ca II K observations and line profiles depends on both the bandwidth employed and observed solar region. As expected, smearing the original data with a spectral kernel leads to greater mixing of photospheric and chromospheric emissions that strongly affects the appearance of the observed regions. In particular, degrading the observations with larger kernels leads to appearance of smaller scale structures and finer details. We found that, among the three regions considered in our study, the one with plages and several small pores shows the largest change in its appearance with the various spectral degradation kernels applied. Moreover, we noticed that the spatial degradation impacts more the data derived from larger bandwidths than those obtained with smaller ones. However, the spatial degradation barely affects the appearance of the solar region observed with bandwidths up to 1 Å, as well as for those observed with a spectral bandwidth in the range $[3,10]$ Å.

Finally, we noticed that the K_3 and $EMDX$ parameters employed for the monitoring of the solar and stellar chromospheric activity vary with the spectral bandwidth as described by a fifth order polynomial function for all the observed solar regions. From the best fitting functions of the data we derived parameters that can be used to intercalibrate results from Ca II K line observations taken with different instruments in diverse regions of the solar atmosphere.

We would like to emphasize that the line intensities reported from our study refer to the specific level of solar magnetism and solar activity framed by the analysed observations. Besides, we note that the analysed data are not representative of all the QS, plages, and sunspot regions of the Sun and other stars. Indeed, regions that appear rather similar at the stellar surface may be characterized by a completely different plasma and magnetic topology at higher atmospheric heights, due to e.g. presence of strong field concentrations in the vicinity of the

analysed region and affecting it. On the other hand, we note that starting from their common doubly-reversed profile, the Ca II H & K lines share many properties being formed in the chromosphere under similar conditions. We thus expect that the findings from our study on the dependence of the Ca II K observations and line profiles on characteristics of the data and observed solar ambient can also qualitatively apply to Ca II H line data.

ACKNOWLEDGMENTS

The authors thank Vincenzo Andretta for useful comments. This study was partly supported by the European Union’s Horizon 2020 research and innovation programme under the grant agreements no. 739500 (PREEST project) and no. 824135 (SOLARNET project), the Italian MIUR-PRIN grant 2017APKP7T on “Circumterrestrial Environment: Impact of Sun-Earth Interaction”, and the Italian agreement ASI-INAF 2021-12-HH.0 “Missione Solar-C EUVST – Supporto scientifico di Fase B/C/D”.

The Swedish 1-m Solar Telescope is operated on the island of La Palma by the Institute for Solar Physics of Stockholm University in the Spanish Observatorio del Roque de los Muchachos of the Instituto de Astrofísica de Canarias.

This research is supported by the Research Council of Norway, project number 325491 and through its Centers of Excellence scheme, project number 262622.

This study has made use of SAO/NASA Astrophysics Data System’s bibliographic services.

REFERENCES

- Esteban Pozuelo, S., de la Cruz Rodríguez, J., Drews, A., et al. 2019, *ApJ*, 870, 88. doi:10.3847/1538-4357/aaf28a
- Bose, S., Henriques, V. M. J., Joshi, J., et al. 2019, *A&A*, 631, L5. doi:10.1051/0004-6361/201936617
- Linsky, J. L. 1968, Ph.D. Thesis
- Murabito, M., Guglielmino, S. L., Ermolli, I., et al. 2021, *A&A*, 653, A93. doi:10.1051/0004-6361/202141034
- Spruit, H. C. 1982, *SoPh*, 75, 3. doi:10.1007/BF00153456
- Solanki, S. K., Riethmüller, T. L., Barthol, P., et al. 2017, *ApJS*, 229, 2. doi:10.3847/1538-4365/229/1/2
- Solanki, S. K., Barthol, P., Danilovic, S., et al. 2010, *ApJL*, 723, L127. doi:10.1088/2041-8205/723/2/L127
- Lites, B. W., Scharmer, G. B., Berger, T. E., et al. 2004, *SoPh*, 221, 65. doi:10.1023/B:SOLA.0000033355.24845.5a
- Leighton, R. B. 1960, *Aerodynamic Phenomena in Stellar Atmospheres*, 12, 321
- Ermolli, I., Giorgi, F., & Chatzistergos, T. 2022, *Frontiers in Astronomy and Space Sciences*, 9, 1042740. doi:10.3389/fspas.2022.1042740
- Chatzistergos, T., Ermolli, I., Krivova, N. A., et al. 2022, *A&A*, 667, A167. doi:10.1051/0004-6361/202244913
- Pötzi, W., Veronig, A., Jarolim, R., et al. 2021, *SoPh*, 296, 164. doi:10.1007/s11207-021-01903-4
- Borucki, W. J., Koch, D., Basri, G., et al. 2010, *Science*, 327, 977. doi:10.1126/science.1185402
- Koch, D. G., Borucki, W. J., Basri, G., et al. 2010, *ApJL*, 713, L79. doi:10.1088/2041-8205/713/2/L79
- Sivaraman, K. R., Singh, J., Bagare, S. P., et al. 1987, *ApJ*, 313, 456. doi:10.1086/164985
- Schou, J., Scherrer, P. H., Bush, R. I., et al. 2012, *SoPh*, 275, 229. doi:10.1007/s11207-011-9842-2
- Scherrer, P. H., Schou, J., Bush, R. I., et al. 2012, *SoPh*, 275, 207. doi:10.1007/s11207-011-9834-2
- Pesnell, W. D., Thompson, B. J., & Chamberlin, P. C. 2012, *SoPh*, 275, 3. doi:10.1007/s11207-011-9841-3
- Tsuneta, S., Ichimoto, K., Katsukawa, Y., et al. 2008, *SoPh*, 249, 167. doi:10.1007/s11207-008-9174-z
- Ichimoto, K., Lites, B., Elmore, D., et al. 2008, *SoPh*, 249, 233. doi:10.1007/s11207-008-9169-9
- Barthol, P., Gandorfer, A., Solanki, S. K., et al. 2011, *SoPh*, 268, 1. doi:10.1007/s11207-010-9662-9
- Martínez Pillet, V., del Toro Iniesta, J. C., Álvarez-Herrero, A., et al. 2011, *SoPh*, 268, 57. doi:10.1007/s11207-010-9644-y
- Scharmer, G. B., Löfdahl, M. G., Sliepen, G., et al. 2019, *A&A*, 626, A55. doi:10.1051/0004-6361/201935735
- Linsky, J. L. 1970, *SoPh*, 11, 355. doi:10.1007/BF00153071
- White, O. R., Livingston, W. C., Keil, S. L., et al. 1998, *Synoptic Solar Physics*, 140, 293
- Linsky, J. L. 2017, *ARA&A*, 55, 159. doi:10.1146/annurev-astro-091916-055327

- Maldonado, J., Phillips, D. F., Dumusque, X., et al. 2019, *A&A*, 627, A118. doi:10.1051/0004-6361/201935233
- Dineva, E., Pearson, J., Ilyin, I., et al. 2022, *Astronomische Nachrichten*, 343, e23996. doi:10.1002/asna.20223996
- Scargle, J. D., Keil, S. L., & Worden, S. P. 2013, *ApJ*, 771, 33. doi:10.1088/0004-637X/771/1/33
- Delbouille, L., Roland, G., & Neven, L. 1973, *Liege: Universite de Liege, Institut d'Astrophysique*, 1973
- Scharmer, G. B., Narayan, G., Hillberg, T., et al. 2008, *ApJL*, 689, L69. doi:10.1086/595744
- Björger, J. P., Sukhorukov, A. V., Leenaarts, J., et al. 2018, *A&A*, 611, A62. doi:10.1051/0004-6361/201731926
- Linsky, J. L. & Avrett, E. H. 1970, *PASP*, 82, 169. doi:10.1086/128904
- Hale, G. E. & Ellerman, F. 1903, *Publications of the Yerkes Observatory*, 3, I.1
- Eberhard, G. & Schwarzschild, K. 1913, *ApJ*, 38, 292. doi:10.1086/142037
- Schmelz, J. T. 2003, *Advances in Space Research*, 32, 895. doi:10.1016/S0273-1177(03)80064-9
- Babcock, H. W. & Babcock, H. D. 1955, *Nature*, 175, 296. doi:10.1038/175296a0
- Howard, R. 1959, *ApJ*, 130, 193. doi:10.1086/146708
- Leighton, R. B. 1959, *ApJ*, 130, 366. doi:10.1086/146727
- Chatzistergos, T., Krivova, N. A., & Ermolli, I. 2022, *Frontiers in Astronomy and Space Sciences*, 9, 1038949. doi:10.3389/fspas.2022.1038949
- Chatzistergos, T., Krivova, N. A., Ermolli, I., et al. 2021, *A&A*, 656, A104. doi:10.1051/0004-6361/202141516
- Chatzistergos, T., Ermolli, I., Krivova, N. A., et al. 2020, *A&A*, 639, A88. doi:10.1051/0004-6361/202037746
- Chatzistergos, T., Ermolli, I., Solanki, S. K., et al. 2019, *A&A*, 626, A114. doi:10.1051/0004-6361/201935131
- Chatzistergos, T., Ermolli, I., Krivova, N. A., et al. 2019, *A&A*, 625, A69. doi:10.1051/0004-6361/201834402
- Chatzistergos, T., Ermolli, I., Solanki, S. K., et al. 2018, *A&A*, 609, A92. doi:10.1051/0004-6361/201731511
- Radick, R. R., Lockwood, G. W., Skiff, B. A., et al. 1998, *ApJS*, 118, 239. doi:10.1086/313135
- Hall, J. C., Lockwood, G. W., & Gibb, E. L. 1995, *ApJ*, 442, 778. doi:10.1086/175483
- Radick, R. R., Lockwood, G. W., Henry, G. W., et al. 2018, *ApJ*, 855, 75. doi:10.3847/1538-4357/aaae3
- Sheeley, N. R. 1967, *SoPh*, 1, 171. doi:10.1007/BF00150852
- White, O. R. & Livingston, W. 1978, *ApJ*, 226, 679. doi:10.1086/156650
- Keil, S. L. & Worden, S. P. 1984, *ApJ*, 276, 766. doi:10.1086/161663
- Noyes, R. W., Hartmann, L. W., Baliunas, S. L., et al. 1984, *ApJ*, 279, 763. doi:10.1086/161945
- Baliunas, S. L. 1984, *NASA Conference Publication*, 2349, 64
- Baliunas, S. L., Donahue, R. A., Soon, W. H., et al. 1995, *ApJ*, 438, 269. doi:10.1086/175072
- Hall, J. C., Lockwood, G. W., & Skiff, B. A. 2007, *AJ*, 133, 862. doi:10.1086/510356
- Wilson, O. C. 1978, *ApJ*, 226, 379. doi:10.1086/156618
- Duncan, D. K., Vaughan, A. H., Wilson, O. C., et al. 1991, *ApJS*, 76, 383. doi:10.1086/191572
- Michel, E., Baglin, A., Auvergne, M., et al. 2008, *Science*, 322, 558. doi:10.1126/science.1163004
- Auvergne, M., Bodin, P., Boisdard, L., et al. 2009, *A&A*, 506, 411. doi:10.1051/0004-6361/200810860
- Gondoin, P., Gandolfi, D., Fridlund, M., et al. 2012, *A&A*, 548, A15. doi:10.1051/0004-6361/201219101
- Sowmya, K., Shapiro, A. I., Witzke, V., et al. 2021, *ApJ*, 914, 21. doi:10.3847/1538-4357/abf247
- Scharmer, G. 2017, *SOLARNET IV: The Physics of the Sun from the Interior to the Outer Atmosphere*, 85
- de la Cruz Rodríguez, J., Löfdahl, M. G., Sütterlin, P., et al. 2015, *A&A*, 573, A40. doi:10.1051/0004-6361/201424319
- Löfdahl, M. G., Hillberg, T., de la Cruz Rodríguez, J., et al. 2021, *A&A*, 653, A68. doi:10.1051/0004-6361/202141326
- Van Noort, M., Rouppe Van Der Voort, L., & Löfdahl, M. G. 2005, *SoPh*, 228, 191. doi:10.1007/s11207-005-5782-z
- Löfdahl, M. G. 2002, *Proc. SPIE*, 4792, 146. doi:10.1117/12.451791
- Kahil, F., Riethmüller, T. L., & Solanki, S. K. 2017, *ApJS*, 229, 12. doi:10.3847/1538-4365/229/1/127
- Wallace, L., Hinkle, K., & Livingston, W. C. 2005, *An atlas of sunspot umbral spectra in the visible from 15,000 to 25,500 cm⁻¹ (3920 to 6664 Å)*, by Wallace, Lloyd.; Hinkle, Kenneth.; Livingston, W. C. [Tucson, AZ : National Solar Observatory, 2005]
- Lefebvre, S., Ulrich, R. K., Webster, L. S., et al. 2005, *Mem. Soc. Astron. Italiana*, 76, 862
- Scharmer, G. B. 2006, *A&A*, 447, 1111. doi:10.1051/0004-6361:20052981
- Lourenço, A., Carvalho, S., Barata, T., et al. 2019, *Open Astronomy*, 28, 165. doi:10.1515/astro-2019-0015
- Chatzistergos, T., Ermolli, I., Solanki, S. K., et al. 2019, *SoPh*, 294, 145. doi:10.1007/s11207-019-1532-5
- Malherbe, J.-M., Bualé, I., Crussaire, D., et al. 2023, *Advances in Space Research*, 71, 1922. doi:10.1016/j.asr.2022.07.058
- Engvold, O., Vial, J.-C., & Skumanich, A. 2019, *The Sun as a Guide to Stellar Physics*, Edited by Oddbjørn Engvold, Jean-Claude Vial and Andrew Skumanich. Elsevier, 2019, ISBN 9780128143346.. doi:10.1016/C2017-0-01365-4

APPENDIX

A. EXAMPLES OF LINE PROFILES

Figure 13 shows examples of line profiles derived from other areas representative of QM and QG features selected nearby the ones reported in Fig. 2. See Sect. 3 for more details.

B. EXAMPLES OF SPECTRALLY AND SPATIALLY DEGRADED DATA

Figure 14 shows examples of original and degraded data for the QS region observed in the red wing of the Ca II K line at $+1.05 \text{ \AA}$ from the line core. Figures 15 and 16 display examples of original and degraded data for the NA observations that include plages and pores, and SP observations with umbral and penumbral regions, respectively. Figure 17 shows examples of CHROMIS observations in the Ca II K line core degraded to the moderate spatial resolution of $4''$ and spectral degradation given by bandwidths in the range $[0.12, 10] \text{ \AA}$, as for the characteristics of most of the existing series of full-disc synoptic solar observations at the Ca II K line. See Sect. 3.2 for more details.

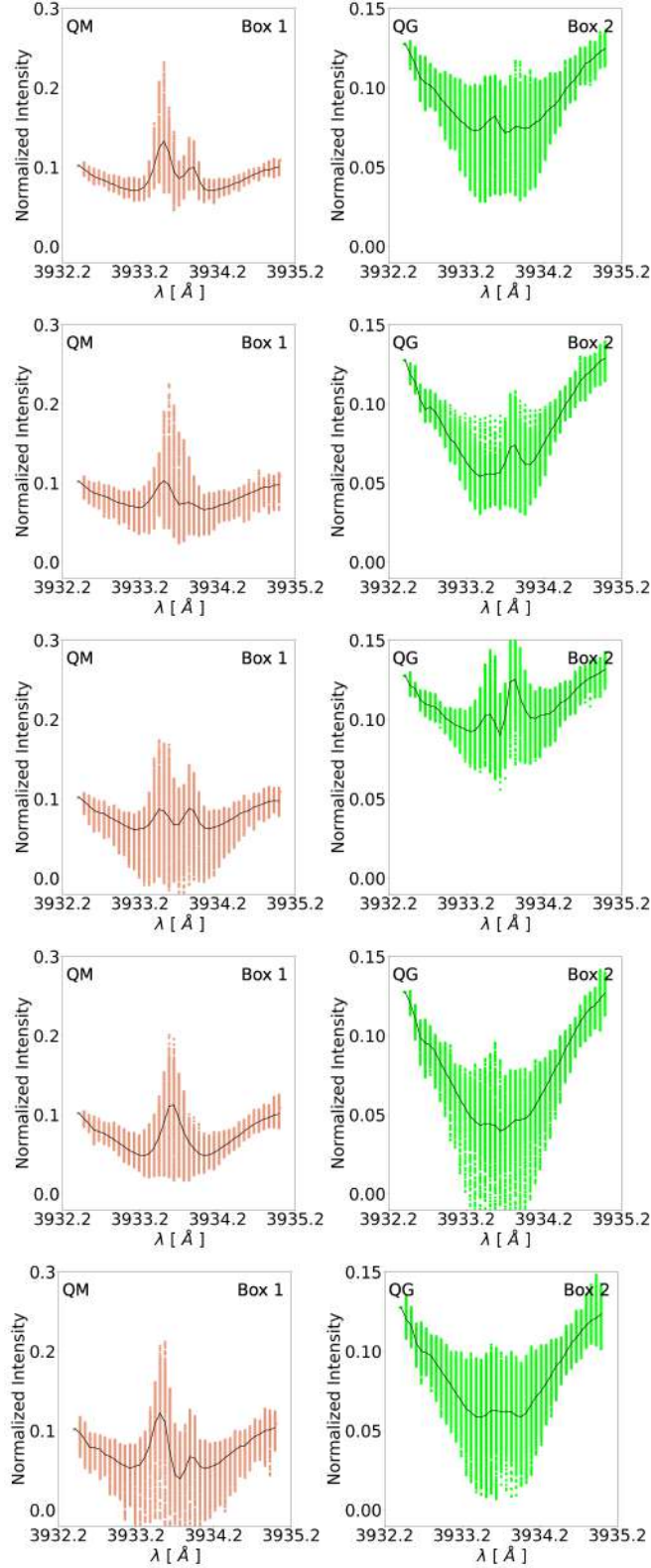


Figure 13. Examples of Ca II K line profiles analysed in our study. These were obtained from 20×20 pixels wide areas overlapping the QM and QG boxes marked with numbers 1 and 2 in Fig. 2 or similar adjacent areas. From top to bottom, panels in each row show results derived from boxes marked in Fig. 2, and from the boxes adjacent to these in their uppermost, lowermost, leftward, and rightward sides, representative of QM (left column panels) and QG (right column panels) regions. Black solid lines show the mean profiles derived from the spatially-resolved data available at each observed spectral position.

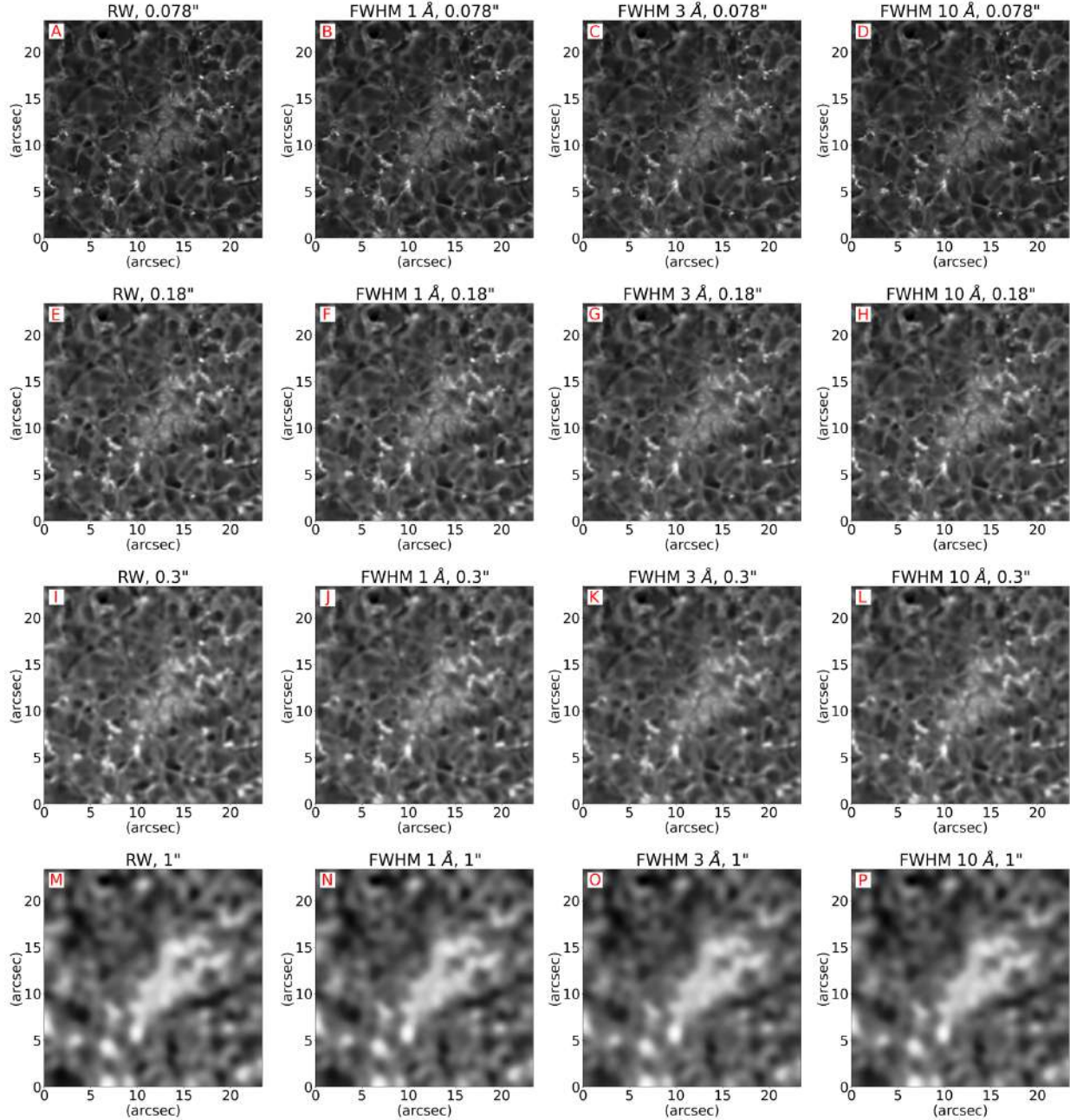


Figure 14. Examples of the original (panel A) and degraded (all other panels) images of the QS region observed in the red wing (RW) at $+1.05 \text{ \AA}$ from the Ca II K line core, to account for the diverse bandwidths and spatial resolutions of the most prominent series of available Ca II K observations. Each row shows examples of data characterized by a given pixel scale and by different bandwidths. From top to bottom, we show data at the original pixel scale of the CHROMIS observations (panels A–D) and degraded to a spatial resolution of $0.18''$ (panels E–H), $0.3''$ (panels I–L), and $1.0''$ (panels M–P), as is in the case of the SUNRISE/IMaX, Hinode/SOT, and SDO/HMI observations, respectively. For each of these observations, from left to right we show the data at the spectral resolution of the CHROMIS observations of 0.12 \AA , and the data spectrally degraded with Gaussian kernels with FWHM of 1, 3, and 10 \AA . Each image is shown using the intensity interval that enhances the visibility of the solar features therein.

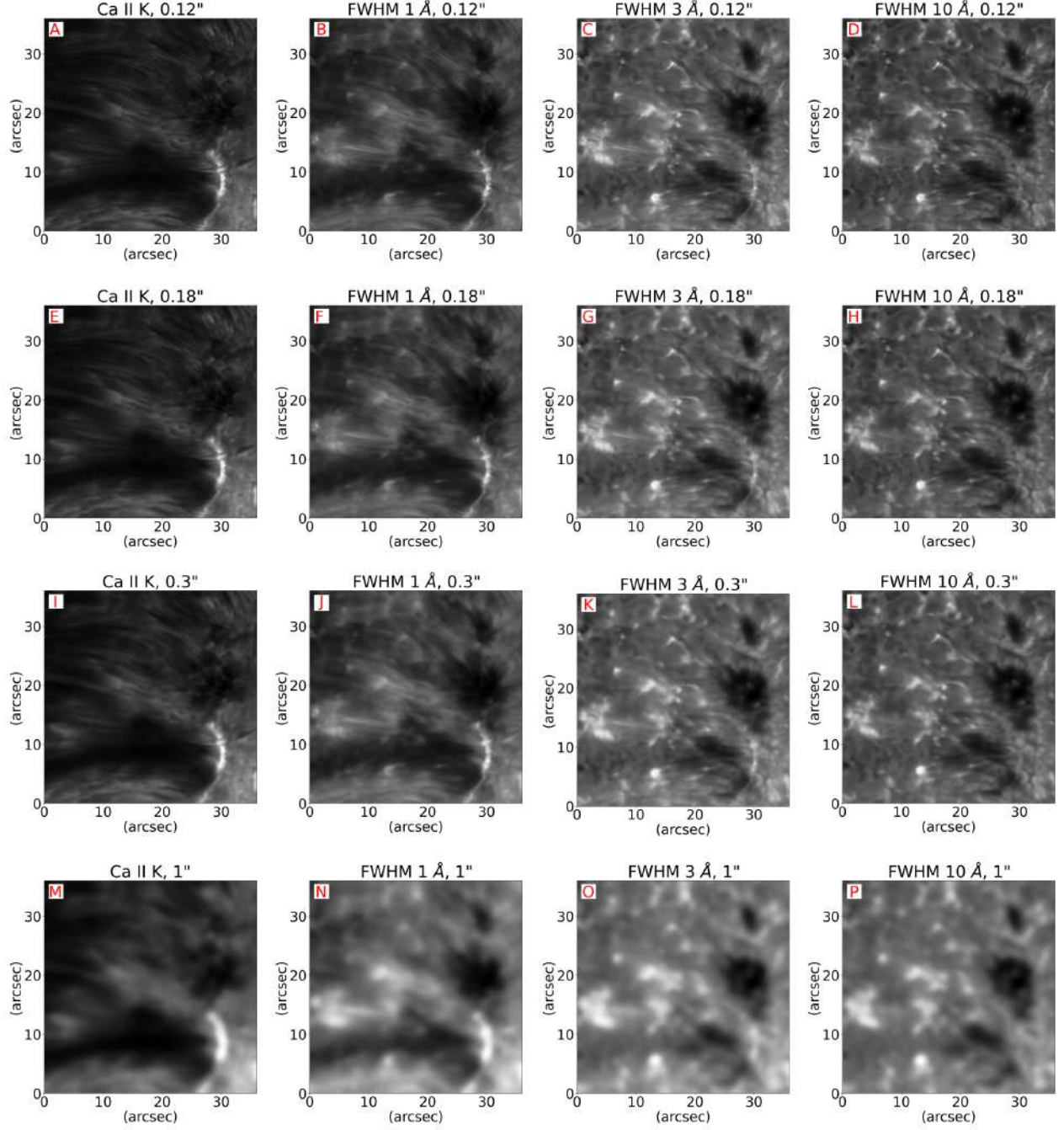


Figure 15. Examples of the original (panel A) and degraded (all other panels) images at the Ca II K line core of the NA region including areas with plagues (PL) and pores (PO), to account for the diverse bandwidths and spatial resolutions of the most prominent series of available Ca II K observations. Each row shows examples of data characterized by a given pixel scale and by different bandwidths. From top to bottom, we show data at the original pixel scale of the CHROMIS observations (panels A–D) and degraded to a spatial resolution of $0.18''$ (panels E–H), $0.3''$ (panels I–L), and $1.0''$ (panels M–P), as is in the case of the SUNRISE/IMaX, Hinode/SOT, and SDO/HMI observations, respectively. For each of these observations, from left to right we show the data at the spectral resolution of the CHROMIS observations of 0.12 \AA , and the data spectrally degraded with Gaussian kernels with FWHM of 1, 3, and 10 \AA . Each image is shown using the intensity interval that enhances the visibility of the solar features therein.

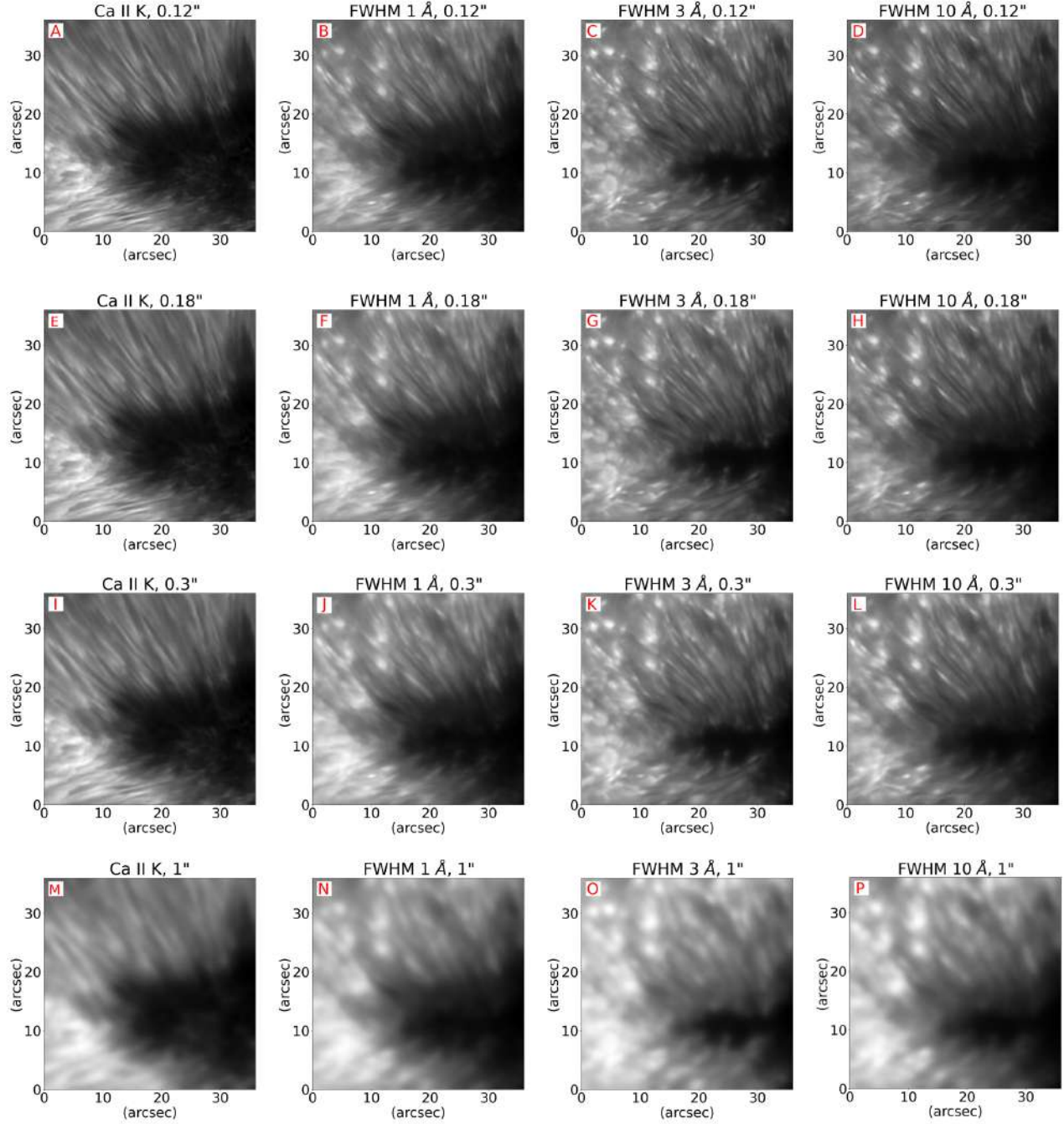


Figure 16. Examples of the original (panel A) and degraded (all other panels) images at the Ca II K line core of the SP region with UM and PE areas, to account for the diverse bandwidths and spatial resolutions of the most prominent series of available Ca II K observations. Each row shows examples of data characterized by a given pixel scale and by different bandwidths. From top to bottom, we show data at the original pixel scale of the CHROMIS observations (panels A–D) and degraded to a spatial resolution of $0.18''$ (panels E–H), $0.3''$ (panels I–L), and $1.0''$ (panels M–P), as is in the case of the pixel scale of the SUNRISE/IMaX, Hinode/SOT, and SDO/HMI observations, respectively. For each of these observations, from left to right we show the data at the spectral resolution of the CHROMIS observations of 0.12 \AA , and the data spectrally degraded with Gaussian kernels with FWHM of 1, 3, and 10 \AA . Each image is shown using the intensity interval that enhances the visibility of the solar features therein.

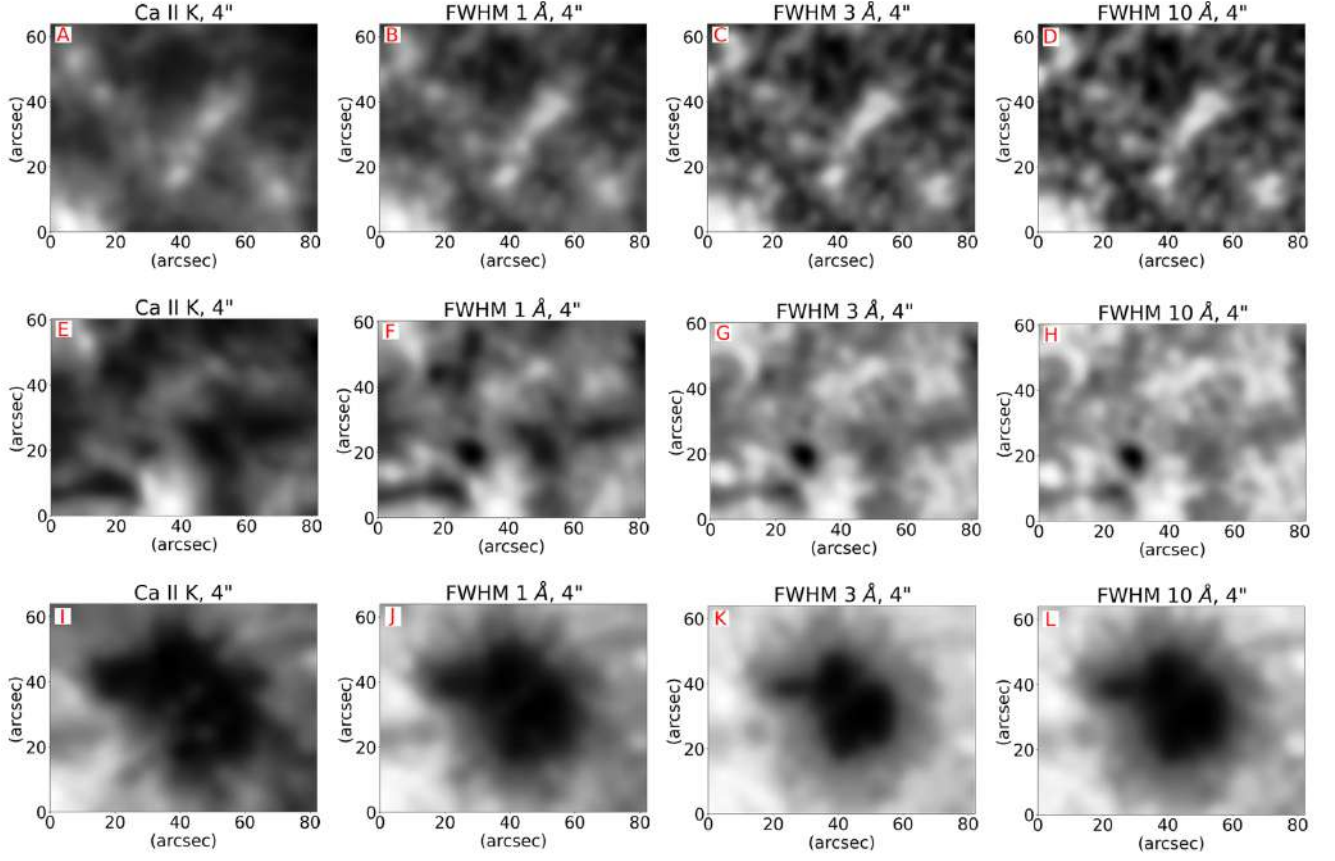


Figure 17. Examples of Ca II K images in the line core degraded to the moderate spatial resolution of $4''$, which meets the characteristics of several existing series of synoptic full-disc solar observations at the Ca II K line, of a quiet Sun area (top row panels), an active region with plages and several pores (middle row panels), and a sunspot with umbra and penumbra (bottom row panels). From left to right the panels in each row show the three regions as observed at the original spectral resolution of the CHROMIS data (0.12 \AA , panels A, E, I), and with bandwidths of 1 \AA (panels B, F, J), 3 \AA (panels C, G, K), and 10 \AA (panels D, H, L). Each image is shown using the intensity interval that enhances the visibility of the solar features therein.